

Cosmological 3D HI Gas Map with HETDEX Ly α Emitters and eBOSS QSOs at $z = 2$:
IGM-Galaxy/QSO Connection and a ~ 40 -Mpc Scale Giant HII Bubble Candidate

SHIRO MUKAE,^{1,2} MASAMI OUCHI,^{3,1,4} GARY J. HILL,^{5,6} KARL GEBHARDT,⁵ ERIN MENTUCH COOPER,⁵ DONGHUI JEONG,^{7,8}
SHUN SAITO,^{9,4} MAXIMILIAN FABRICIUS,^{10,11} ERIC GAWISER,¹² ROBIN CIARDULLO,^{7,8} DANIEL FARROW,¹⁰ DUSTIN DAVIS,⁵
GREG ZEIMANN,¹³ STEVEN L. FINKELSTEIN,⁵ CARYL GRONWALL,^{7,8} CHENXU LIU,⁵ YECHEI ZHANG,^{1,2} CHRIS BYROHL,¹⁴
YOSHIKI ONO,¹ DONALD P. SCHNEIDER,^{7,8} MATT J. JARVIS,^{15,16} CAITLIN M. CASEY,⁵ AND KEN MAWATARI¹

¹ *Institute for Cosmic Ray Research, The University of Tokyo, 5-1-5 Kashiwanoha, Kashiwa, Chiba 277-8582, Japan*

² *Department of Astronomy, Graduate School of Science, The University of Tokyo, 7-3-1 Hongo, Bunkyo, Tokyo, 113-0033, Japan*

³ *National Astronomical Observatory of Japan, 2-21-1 Osawa, Mitaka, Tokyo 181-8588, Japan*

⁴ *Kavli Institute for the Physics and Mathematics of the Universe (Kavli IPMU, WPI), The University of Tokyo, 5-1-5 Kashiwanoha, Kashiwa, Chiba, 277-8583, Japan*

⁵ *Department of Astronomy, The University of Texas at Austin, 2515 Speedway, Stop C1400, Austin, Texas 78712, USA*

⁶ *McDonald Observatory, University of Texas at Austin, 2515 Speedway, Stop C1402, Austin, TX 78712, USA*

⁷ *Department of Astronomy and Astrophysics, The Pennsylvania State University, University Park, PA 16802*

⁸ *Institute for Gravitation and the Cosmos, The Pennsylvania State University, University Park, PA 16802*

⁹ *Institute for Multi-messenger Astrophysics and Cosmology, Department of Physics, Missouri University of Science and Technology, 1315 N. Pine Street, Rolla, MO 65409, USA*

¹⁰ *Max-Planck-Institut für extraterrestrische Physik, Giessenbachstrasse, D-85748 Garching, Germany*

¹¹ *Universitäts-Sternwarte München, Scheinerstrasse 1, D-81679 München, Germany*

¹² *Department of Physics and Astronomy, Rutgers University, Piscataway, NJ 08854, USA*

¹³ *Hobby Eberly Telescope, University of Texas, Austin, TX 78712, USA*

¹⁴ *Max-Planck-Institut für Astrophysik, Karl-Schwarzschild-Str. 1, D-85748 Garching, Germany*

¹⁵ *Astrophysics, Department of Physics, Keble Road, Oxford, OX1 3RH, UK*

¹⁶ *Department of Physics & Astronomy, University of the WesternCape, Private Bag X17, Bellville, Cape Town, 7535, South Africa*

(Accepted for Publication in ApJ)

ABSTRACT

We present cosmological (30 – 400 Mpc) distributions of neutral hydrogen (HI) in the inter-galactic medium (IGM) traced by Ly α Emitters (LAEs) and QSOs at $z = 2.1 - 2.5$, selected with the data of the on-going Hobby-Eberly Telescope Dark Energy Experiment (HETDEX) and the eBOSS survey. Motivated by a previous study of Mukae et al. (2020), we investigate spatial correlations of LAEs and QSOs with HI tomography maps reconstructed from HI Ly α forest absorption in the spectra of background galaxies and QSOs obtained by the CLAMATO survey and this study, respectively. In the cosmological volume far from QSOs, we find that LAEs reside in regions of strong HI absorption, i.e. HI rich, which is consistent with results of previous galaxy-background QSO pair studies. Moreover, there is an anisotropy in the HI-distribution plot of transverse and line-of-sight distances; on average the HI absorption peak is blueshifted by ~ 200 km s⁻¹ from the LAE Ly α redshift, reproducing the known average velocity offset between the Ly α emission redshift and the galaxy systemic redshift. We have identified a ~ 40 -Mpc scale volume of HI underdensity that is a candidate for a giant HII bubble, where six QSOs and an LAE overdensity exist at $\langle z \rangle = 2.16$. The coincidence of the QSO and LAE overdensities with the HI underdensity indicates that the ionizing photon radiation of the QSOs has created a highly ionized volume of multiple proximity zones in a matter overdensity. Our results suggest an evolutionary picture where HI gas in an overdensity of galaxies becomes highly photoionized when QSOs emerge in the galaxies.

Keywords: galaxies: formation — intergalactic medium — large-scale structure of universe

1. INTRODUCTION

In the modern paradigm of galaxy formation, galaxies form and evolve in gaseous filamentary structures

(e.g., Mo et al. 2010; Meiksin 2009). Studies of cosmological hydrodynamics simulations have suggested a picture where galaxies and the gaseous large-scale structures (LSSs) exchange baryonic gas by gas flows (Fox & Davé 2017; van de Voort 2017). Cold gas ($\sim 10^4$ K) in the intergalactic medium (IGM) accretes onto galaxies through the filamentary structures, and triggers star formation in the galaxies (e.g., Dekel et al. 2009; Kereš et al. 2005). Star formation heats up the gas, and the gas is expelled from the galaxies by feedback processes such as galactic outflows (e.g., Somerville & Davé 2015; Viel et al. 2013). Observing the site of the gas exchange is key for understanding galaxy formation in gaseous LSSs, especially at $z \sim 2 - 3$ when the star-formation rate density peaks in cosmic history. However, the connections between galaxies and gaseous LSSs are as yet poorly probed in observations.

To study galaxy formation in gaseous LSSs, recent observational studies have probed the IGM neutral hydrogen (HI) at $z \sim 2 - 3$, revealing the spatial distribution of the HI Ly α forest absorption (HI absorption). Until a decade ago, HI-gas distributions around galaxies were studied by stacking analyses of background QSO spectra in which the HI-gas of foreground galaxies causes weak absorption (e.g., Adelberger et al. 2005; Turner et al. 2014; Bielby et al. 2017). The measurements of stacked spectra have shown HI absorption as a function of transverse distance to the background QSO sightline, and revealed an HI absorption excess around massive star-forming galaxies over $\sim 5 h^{-1}$ comoving Mpc (h^{-1} cMpc). However, the stacked HI-gas distributions are based on measurements in multiple fields, and represent the cosmic-averaged distribution, losing information on specific galaxy environments such as overdensities of galaxies and QSOs.

In the past few years, Lee et al. (2014b) have observationally demonstrated a HI tomography technique that reconstructs three dimensional (3D) HI LSSs at $z \sim 2$ from HI absorption found in multiple background galaxy spectra. The HI tomography technique was originally proposed by Pichon et al. (2001) and Caucci et al. (2008) for the purpose of recovering the large-scale topology of the underlying matter field. The observational requirements of HI tomography are investigated by Lee et al. (2014a) for 8–10m-class telescopes and by Steidel et al. 2009 and Evans et al. 2012, for those of 30 m-class. The subsequent HI tomography studies of Lee et al. (2016, 2018) have revealed HI LSSs with spatial resolutions of $2.5 h^{-1}$ cMpc in the COSMOS Ly α Mapping And Tomography Observations (CLAMATO) survey. Although the HI tomography technique has enabled spatial characterization of HI LSSs in a field of interest, only a few studies systematically investigate connections between HI LSSs and galaxies in a range of environments from blank fields (that are randomly selected extra-galactic survey fields) to specific fields such as galaxy overdensities (Mukae et al. 2020; Newman et al. 2020).

As a wide-field and statistical study complementary to the CLAMATO survey, Mukae et al. (2017) have investigated spatial correlations of average HI-gas overdensities and galaxy overdensities at $z \sim 2 - 3$, using galaxy photometry and multiple spectra of background QSOs in a large 1.62 deg^2 area of the COSMOS/UltraVISTA field. The spatial correlation results suggest that a large amount of HI-gas is associated with galaxy overdensities (see also Liang et al. 2020; Nagamine et al. 2020). However, it is still unknown how the distribution of the HI LSSs is affected by overdensities of galaxies and QSOs on an individual structure basis. Because QSOs often emerge in galaxy overdensities, the QSOs’ radiation can enhance the ultraviolet background (UVB) radiation in the overdensities, photo-ionizing the surrounding HI-gas (e.g., Umehata et al. 2019; Kikuta et al. 2019). These QSO photoionization regions are dubbed proximity zones whose sizes are observationally estimated to be $\sim 10 - 15 h^{-1}$ cMpc in diameter at $z \sim 2$ (e.g., D’Odorico et al. 2008; Mukae et al. 2020; Jalan et al. 2019). Moreover, enhanced UVB radiation can suppress star formation of galaxies in low-mass dark matter halos by photo-evaporation of their gas (e.g., Susa & Umemura 2004, 2000), which is implied by observational studies of galaxy number counts around QSOs (e.g., Kashikawa et al. 2007; Kikuta et al. 2017). The three key elements for galaxy formation in LSSs are dark matter, gas, and ionization. To understand the impact of overdensities of galaxies and QSOs on the surrounding gas, systematic study the HI-gas distributions around galaxies in various galaxy environments is required.

In this study, we investigate IGM HI-gas distributions around galaxies at $z \sim 2$ in the following two galaxy environments: a blank field (i.e. a randomly selected extra-galactic survey field) and an extreme QSO overdensity region. We use the large datasets of galaxies and QSOs consisting of the spectroscopic data of the Hobby-Eberly Telescope Dark Energy Experiment (HETDEX; Hill et al. 2008; Hill & HETDEX Consortium 2016, Gebhardt et al. 2020, in preparation) and the extended Baryon Oscillation Spectroscopic Survey of the Sloan Digital Sky Survey IV (SDSS-IV/eBOSS; Dawson et al. 2016), respectively. To probe IGM HI-gas distributions at $z \sim 2$, we use HI absorption found in spectra of background QSOs at $z > 2$. We perform HI tomography based on the multiple HI absorptions, to reveal 3D HI LSSs around the galaxies.

The structure of this paper is as follows. In Section 2, we describe our datasets of foreground/background galaxies and QSOs. In Section 3, we detail our HI tomography techniques and our HI tomography maps. We present results and discussion in Sections 4 and 5, respectively. In Section 6, we summarize our major findings. Throughout this paper, we use a cosmological parameter set: $(\Omega_m, \Omega_\Lambda, \Omega_b, h) = (0.26, 0.74, 0.045, 0.70)$ consistent with the nine-year WMAP result (Hinshaw et al. 2013). We refer to kpc and Mpc in comoving

(physical) units as ckpc and cMpc (pkpc and pMpc), respectively. We specifically use units including h^{-1} for ckpc and cMpc, because these units are widely found in this field of study, and allow readers to easily compare our results with previous ones. All magnitudes are in AB magnitudes (Oke & Gunn 1983).

2. GALAXY AND QSO CATALOGS

We investigate IGM HI-gas distributions around $z \sim 2$ galaxies in two fields shown in Sections 4.1 and 4.2, respectively:

- COSMOS: a blank field of 0.157 deg^2 with no extreme overdensities that is placed around the center of the CLAMATO survey (Lee et al. 2018)
- EGS: a field of 6.0 deg^2 that is a combination of the original and flanking EGS (Davis et al. 2007) regions. Although this is a blank field (i.e. a randomly selected extra-galactic survey field), it contains a significant QSO overdensity (Section 4.2).

We describe our galaxy (i.e. LAE) and QSO catalogs in Sections 2.1 and 2.2, respectively. The QSO catalogs contain foreground and background QSOs (Sections 2.2.1-2.2.2). The background QSOs are used for probing HI absorption via an HI tomography map covering $z = 2.05 - 2.55$, while the foreground QSOs are those included in a cosmic volume of the HI tomography map. Note that, throughout this paper, we use the words ‘foreground’ and ‘background’ for sources located in the HI tomography maps and for those utilized to create the HI tomography map, respectively.¹ Table 1 summarizes the data sources for the galaxies and QSOs.

2.1. LAE Catalogs

Two catalogs of foreground galaxies are drawn from samples of $\text{Ly}\alpha$ emitters (LAEs) in the COSMOS and EGS regions. The COSMOS and EGS LAE catalogs are constructed from early observations of HETDEX, obtained with the Visible Integral-field Replicable Unit Spectrograph (VIRUS, Hill et al. 2018a) on the upgraded 10 m Hobby-Eberly Telescope (HET). The HET (Ramsey et al. 1994; Hill et al. 2018b) is an innovative telescope with 11-meter segmented primary mirror, located in West Texas at the McDonald Observatory. VIRUS is a massively replicated integral field spectrograph (Hill 2014), designed for blind spectroscopic surveys. It consists of 78 fiber integral field units (IFUs;

Kelz et al. 2014) distributed within the 22 arcmin diameter field of view of the telescope. A detailed technical description of the HET wide field upgrade and VIRUS is presented in Hill et al. (2020, in preparation).² Each IFU feeds 448 fibers with diameter $1''5$ to a pair of spectrographs. The spectrographs have a fixed spectral bandpass of $\lambda = 3500\text{--}5500 \text{ \AA}$ and a spectral resolution of $R \approx 800$. The HETDEX program is performing a blind emission line survey over a total of $\sim 450 \text{ deg}^2$ area with a standard exposure set of $6 \text{ min} \times 3$ dithers (to fill the sky gaps between fibers), and aims to identify 10^6 LAEs at $\text{Ly}\alpha$ -emission redshifts of $z_{\text{Ly}\alpha} = 1.9\text{--}3.5$ in a 9 Gpc^3 volume. The HETDEX survey constructs an emission-line database (Gebhardt et al. 2020, in preparation) where emission-line detections are processed in combination with broadband imaging data, including data from Subaru/Hyper Suprime-Cam (HSC) (Gebhardt et al. 2020 in preparation).

We choose 27 (26) spectroscopically identified LAEs in the COSMOS (EGS) field by the following three criteria: i) a single emission-line is detected with a significance level greater than 6.5σ as defined by the HETDEX line-identification algorithm (Gebhardt et al. 2020, in preparation) that considers the fiber filling factor within the IFUs of 1/3, ii) a high observed equivalent width of the single emission line and a low luminosity, distinguishing high- z $\text{Ly}\alpha$ from low- z [OII] emission with Bayesian statistics whose prior distributions are given by previous optical spectroscopic results with a wide-wavelength coverage (Leung et al. 2017), iii) the total luminosity of the $\text{Ly}\alpha$ emission is $L_{\text{Ly}\alpha} > 10^{42.8} \text{ erg s}^{-1}$, which achieves source identification completeness of $\gtrsim 90\%$ (Gebhardt et al. 2020, in preparation; Zhang et al. in preparation), and iv) the redshift of the $\text{Ly}\alpha$ emission line falls in the range of $z_{\text{Ly}\alpha} = 2.05\text{--}2.55$. The redshift range is chosen to match with that of the COSMOS HI tomography map (Lee et al. 2018, Section 3.2.1). Figures 1 and 2 (Figures 3 and 4) present the sky (redshift and luminosity) distributions of our HETDEX LAEs in the COSMOS and EGS fields, respectively. The basic properties of the HETDEX LAEs in the COSMOS and EGS fields are summarized in Tables 2 and 3, respectively.

2.2. QSO Catalogs

2.2.1. Foreground QSOs

The foreground QSOs in our samples are taken from the DR14 QSO catalog (hereafter DR14Q; Pâris et al. 2018) of SDSS-IV/eBOSS spectra that have a spectral resolution and coverage of $R \approx 2000$ and $3600\text{--}10400 \text{ \AA}$,

¹ Although the background sources reside at $z = 2.1 - 3.1$, the redshift range of $\text{Ly}\alpha$ forest absorption contributing to the HI tomography map construction depends on the background-source redshift. This is because $\text{Ly}\alpha$ forest absorption over rest-frame wavelengths $1041 - 1185 \text{ \AA}$ is used for the HI tomography mapping. For this reason, we do not associate a particular redshift range with the background sources, but use the term ‘background’ throughout the paper.

² The VIRUS array has been undergoing staged deployment of IFUs and spectrograph units starting in late 2015. The data presented in this paper were obtained with between 16 and 47 active IFUs, with up to 21,056 fibers and were observed between January 3, 2017 to February 09, 2019.

COSMOS

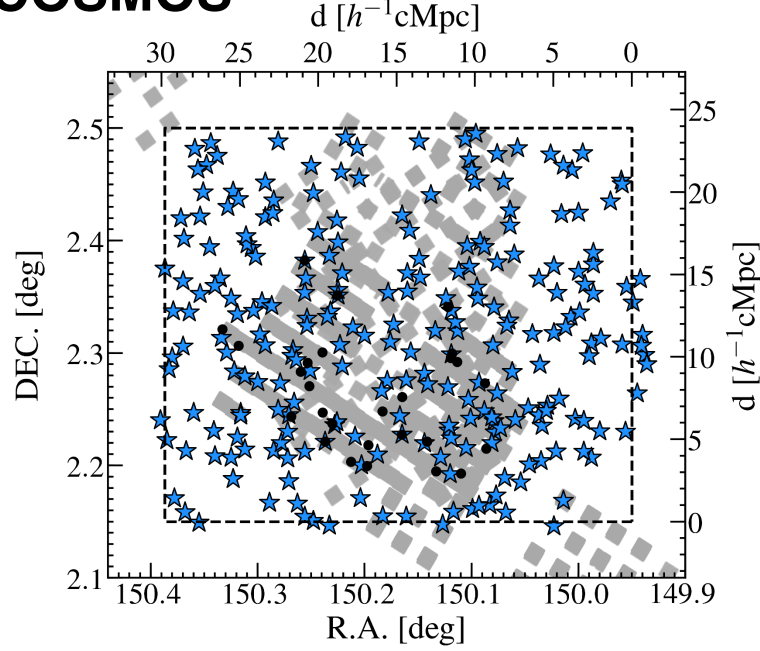


Figure 1. Sky distribution of galaxies and QSOs in the 0.157 deg^2 area of the COSMOS field. The blue stars represent the positions of background objects that are used for HI tomography mapping (Lee et al. 2018). The black dots are the foreground galaxies, HETDEX LAEs, at $z = 2.05\text{--}2.55$ (Section 2.1). Note that no foreground QSOs are found in this moderately small area of the COSMOS field. The gray shaded squares present the area covered by the IFUs of the HETDEX survey. The dashed-line box indicates the COSMOS field for the HI tomography map whose spatial resolution is $2.5 h^{-1} \text{ cMpc}$ (Section 3.2.1). The axes on the top and right-hand side indicate the projected comoving scale at $z = 2.3$.

EGS

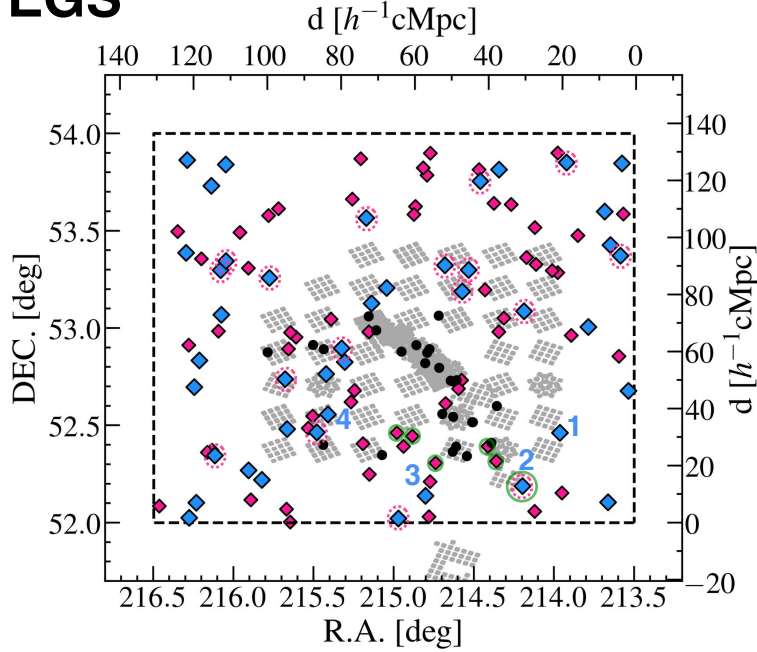


Figure 2. Sky distribution of foreground and background QSOs in the 6.0 deg^2 area of the EGS field. The blue diamonds are the positions of the background QSOs (Section 2.2.2). The background QSO sightlines 1-4 probe a large HI underdensity (Section 4.2) and their spectra are presented in Figure 14. The magenta diamonds are the positions of foreground QSOs at $z = 2.05\text{--}2.55$ (Section 2.2.1). The magenta dotted circles indicate the background QSOs that are also used as foreground QSOs (Section 4.2). The green circles represent six QSOs comprising the extreme QSO overdensity, EGS-QO1 (Section 4.2). The black dots are HETDEX LAEs at $z = 2.05\text{--}2.55$ (Section 2.1). The gray shaded squares present the area covered by the IFUs of the HETDEX survey. The dashed-line box is the EGS field for the HI tomography map whose spatial resolution is $20 h^{-1} \text{ cMpc}$ (Section 3.2.2). The axes on the top and right-hand side indicate the projected comoving scale at $z = 2.3$.

Table 1. Data Summary of the Two Fields

Field	Area (deg ²)	Volume (h^{-3} cMpc ³)	Galaxy Sample	QSO Sample	HI Map
COSMOS	0.157	3.2×10^5	HETDEX	eBOSS	Lee et al. (2018)
EGS	6.0	7.5×10^6 [†]	HETDEX	eBOSS	This Study

[†] In EGS, the QSO overdensity EGS-QO1 (Section 4.2) occupies a volume of $1.1 \times 10^5 h^{-3} \text{ cMpc}^3$.

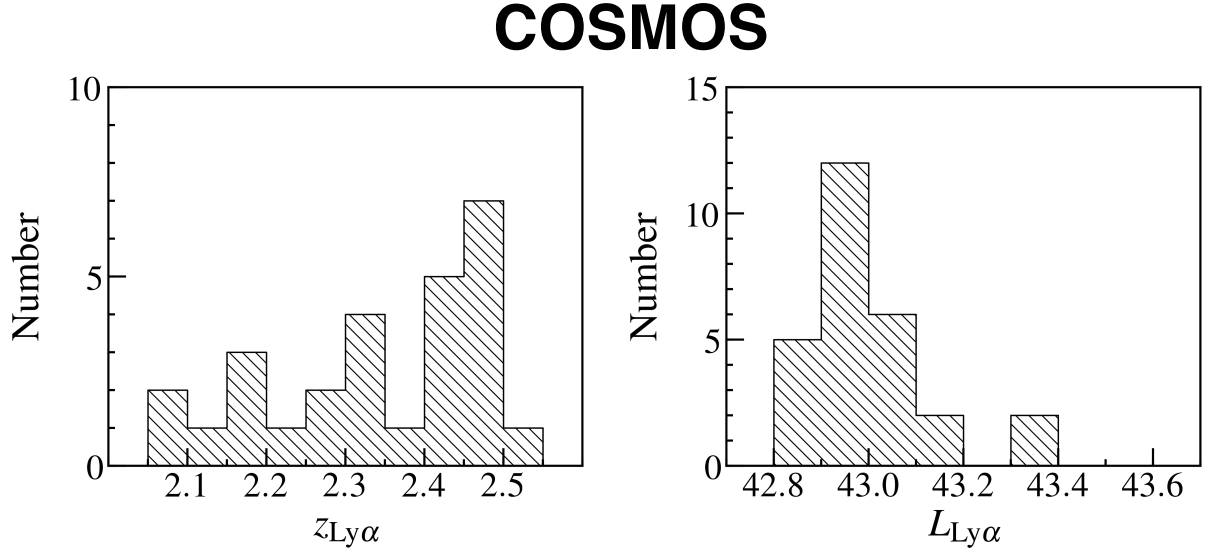
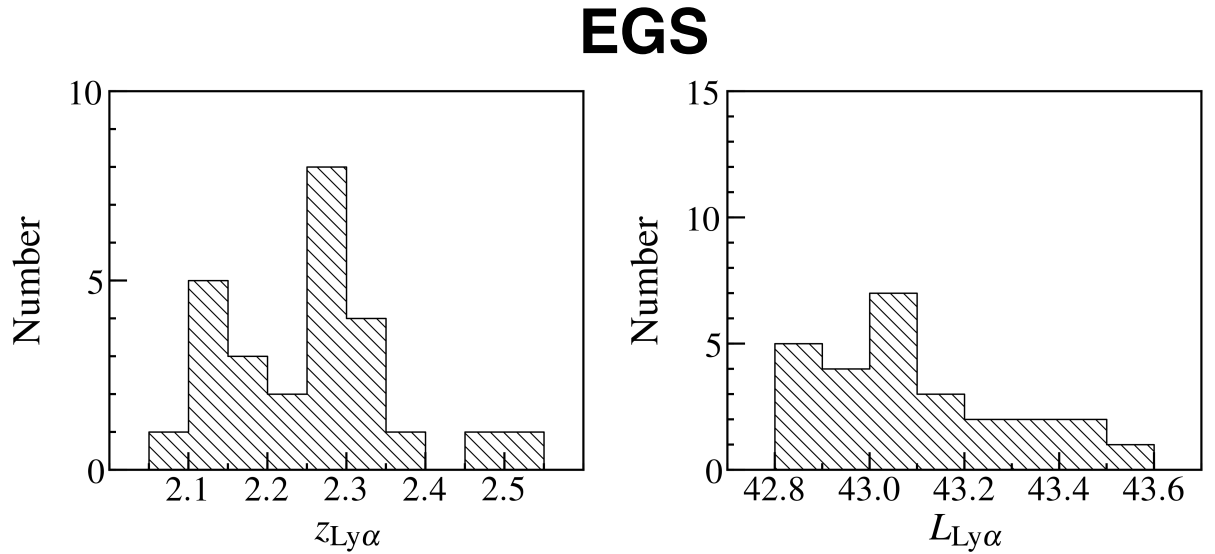
**Figure 3.** $z_{\text{Ly}\alpha}$ (left) and $L_{\text{Ly}\alpha}$ (right) distributions of 27 HETDEX LAEs in the 0.157 deg² area of the COSMOS field.**Figure 4.** $z_{\text{Ly}\alpha}$ (left) and $L_{\text{Ly}\alpha}$ (right) distributions of 26 HETDEX LAEs in the 6.0 deg² area of the EGS field.

Table 2. HETDEX LAEs in the COSMOS field

ID	R.A.	Decl.	$z_{\text{Ly}\alpha}$	$L_{\text{Ly}\alpha}$
	(J2000)	(J2000)		($10^{42} \text{ erg s}^{-1}$)
HETDEX J100028.34+021758.5	10:00:28.34	+02:17:58.50	2.492	9.28
HETDEX J100051.07+021211.9	10:00:51.07	+02:12:11.94	2.444	11.42
HETDEX J100043.97+021452.8	10:00:43.97	+02:14:52.76	2.486	24.69
HETDEX J100020.68+021253.3	10:00:20.68	+02:12:53.32	2.156	8.47
HETDEX J100116.29+021823.0	10:01:16.29	+02:18:23.04	2.322	7.56
HETDEX J100031.95+021140.8	10:00:31.95	+02:11:40.80	2.198	8.72
HETDEX J100056.83+021316.3	10:00:56.83	+02:13:16.32	2.433	13.23
HETDEX J100102.35+021659.9	10:01:02.35	+02:16:59.89	2.508	19.97
HETDEX J100054.09+022104.8	10:00:54.09	+02:21:04.80	2.472	9.34
HETDEX J100104.47+021436.5	10:01:04.47	+02:14:36.50	2.139	6.58
HETDEX J100057.47+021801.7	10:00:57.47	+02:18:01.68	2.163	10.05
HETDEX J100021.01+021622.9	10:00:21.01	+02:16:22.92	2.441	8.35
HETDEX J100119.92+021915.8	10:01:19.92	+02:19:15.82	2.323	9.43
HETDEX J100100.42+021613.9	10:01:00.42	+02:16:13.86	2.099	7.23
HETDEX J100047.46+021158.1	10:00:47.46	+02:11:58.05	2.282	8.51
HETDEX J100039.54+021539.0	10:00:39.54	+02:15:38.96	2.453	10.89
HETDEX J100028.65+021744.0	10:00:28.65	+02:17:44.05	2.099	9.47
HETDEX J100101.45+022256.5	10:01:01.45	+02:22:56.51	2.320	6.34
HETDEX J100047.17+021305.1	10:00:47.17	+02:13:05.06	2.340	9.58
HETDEX J100027.22+021731.5	10:00:27.22	+02:17:31.47	2.287	11.31
HETDEX J100100.82+021728.7	10:01:00.82	+02:17:28.67	2.470	9.31
HETDEX J100026.37+021134.2	10:00:26.37	+02:11:34.22	2.376	11.97
HETDEX J100029.24+022027.3	10:00:29.24	+02:20:27.27	2.467	13.17
HETDEX J100057.43+021449.5	10:00:57.43	+02:14:49.48	2.499	7.41
HETDEX J100033.97+021316.2	10:00:33.97	+02:13:16.15	2.230	9.26
HETDEX J100055.21+021413.7	10:00:55.21	+02:14:13.67	2.414	9.21
HETDEX J100039.63+021338.3	10:00:39.63	+02:13:38.35	2.441	11.37

respectively. In this study, we use foreground QSOs in the cosmic volumes of our HI tomography maps (Section 3.2). We select foreground QSOs from DR14Q in the redshift range $z = 2.05 - 2.55$ in the 0.157 and 6.0 deg² sky areas of the COSMOS and EGS fields, and find a total of 0 and 78 QSOs, respectively. Figure 2 presents the sky distribution of the foreground QSOs in the EGS field. The basic properties of the foreground QSOs in the EGS field are summarized in Tables 4 and 5.

2.2.2. Background QSOs

The background QSOs are also taken from the DR14Q catalog. We only make a sample of background QSOs in the EGS field. This is because we do not need to use background QSOs for the HI tomography map in the COSMOS field, where a high-resolution HI tomography map is already available (Section 3.2.1). We select back-

ground QSOs from DR14Q in the redshift range $z = 2.1 - 3.1$ in the 6.0 deg² sky area of the EGS field. The redshift range of $z = 2.1 - 3.1$ is chosen, because we aim to investigate the HI Ly α forest of foreground absorbers in the same redshift range as those of the COSMOS HI tomography map ($z = 2.05 - 2.55$; Section 3.2.1). We apply these two criteria, and obtain 128 background QSOs.

For our analysis of HI Ly α forest absorption, we investigate these QSO spectra, and conduct further selection. We apply a criterion that QSO spectra should have a median signal-to-noise ratio (S/N) ≥ 2 per pixel over their Ly α forest wavelength range (i.e., 1041–1185 Å in the rest-frame; Mukae et al. 2017). In addition, we remove QSOs whose spectra have broad absorption lines whose BALnicity Index (BI) blueward of C IV emission is BI $< 200 \text{ km s}^{-1}$ in the DR14Q catalog. We also remove QSOs with a damped Ly α system (DLA) in the Ly α for-

Table 3. HETDEX LAEs in the EGS field

ID	R.A.	Decl.	$z_{\text{Ly}\alpha}$	$L_{\text{Ly}\alpha}$	Label ^a
	(J2000)	(J2000)		($10^{42} \text{ erg s}^{-1}$)	
HETDEX J141948.50+525246.9	14:19:48.50	+52:52:46.85	2.206	9.85	-
HETDEX J141909.77+525223.4	14:19:09.77	+52:52:23.38	2.296	11.98	-
HETDEX J141851.86+524745.9	14:18:51.86	+52:47:45.85	2.451	7.58	-
HETDEX J141913.02+524911.2	14:19:13.02	+52:49:11.23	2.156	11.38	LAE4
HETDEX J141906.49+525328.0	14:19:06.49	+52:53:27.98	2.531	6.33	-
HETDEX J141926.25+525441.9	14:19:26.25	+52:54:41.95	2.291	13.89	-
HETDEX J142017.52+522050.5	14:20:17.52	+52:20:50.55	2.298	30.32	-
HETDEX J141725.63+523557.5	14:17:25.63	+52:35:57.51	2.298	9.79	-
HETDEX J141810.58+522031.2	14:18:10.58	+52:20:31.17	2.103	13.52	-
HETDEX J141826.73+522329.7	14:18:26.73	+52:23:29.71	2.308	12.46	-
HETDEX J141831.80+522154.0	14:18:31.80	+52:21:53.96	2.348	12.53	-
HETDEX J141733.68+522437.8	14:17:33.68	+52:24:37.79	2.147	10.49	LAE1
HETDEX J141801.61+523101.0	14:18:01.61	+52:31:00.99	2.103	26.78	-
HETDEX J141802.49+523100.0	14:18:02.49	+52:31:00.01	2.103	6.96	-
HETDEX J141831.12+523239.7	14:18:31.12	+52:32:39.69	2.141	22.68	LAE2
HETDEX J141847.24+523329.5	14:18:47.24	+52:33:29.49	2.302	9.29	-
HETDEX J142145.41+522401.2	14:21:45.41	+52:24:01.16	2.175	39.25	-
HETDEX J141852.67+530350.6	14:18:52.67	+53:03:50.64	2.254	11.19	-
HETDEX J142308.86+525232.6	14:23:08.86	+52:52:32.56	2.246	20.83	-
HETDEX J141825.85+524355.4	14:18:25.85	+52:43:55.41	2.297	6.50	-
HETDEX J141834.58+524346.0	14:18:34.58	+52:43:45.97	2.188	10.69	LAE3
HETDEX J142144.85+525330.0	14:21:44.85	+52:53:30.01	2.341	13.29	-
HETDEX J142200.64+525448.7	14:22:00.64	+52:54:48.73	2.355	9.08	-
HETDEX J141830.26+524329.8	14:18:30.26	+52:43:29.82	2.299	17.33	-
HETDEX J142026.24+525919.4	14:20:26.24	+52:59:19.36	2.289	7.90	-
HETDEX J142037.65+530335.6	14:20:37.65	+53:03:35.62	2.055	17.85	-

^a LAEs 1–4 reside in the QSO overdensity, EGS-QO1 (Section 4.2).

est wavelength range on the basis of the DLA catalog of Noterdaeme et al. (2012) and their updated one³ for the SDSS DR12 QSOs (Pâris et al. 2017). For QSOs that have no SDSS DR12 counterpart, we visually inspect the QSO spectra, and examine whether signatures of DLAs exist in the $\text{Ly}\alpha$ forest wavelength range.

Our selection gives a total of 43 background QSOs for the HI tomography analysis. The distribution of the background QSOs is shown in Figure 2. The basic properties of the 43 background QSOs are summarized in Table 6. Some example QSO spectra are shown in Figure 5.

3. HI TOMOGRAPHY TECHNIQUES AND MAPS

We carry out HI tomography mapping that is a technique to reconstruct the 3D HI LSSs based on HI absorption features found in the sightlines to multiple background source spectra (e.g., Lee et al. 2018, 2014b,a; Caucci et al. 2008; Pichon et al. 2001). This Section describes how we make HI tomography maps from background source spectra (Section 3.1), and presents HI tomography maps of the COSMOS and EGS fields (Section 3.2). Note that we make a new HI tomography map only in the EGS field. This is because we use the public data of the HI tomography map in the COSMOS field (Lee et al. 2018, Section 3.2.1).

3.1. HI Tomography Techniques

³ <http://www2.iap.fr/users/noterdae/DLA/DLA.html>

Table 4. Foreground QSOs in the EGS field

ID	R.A. (J2000)	Decl. (J2000)	z_{spec}
7339-56722-0728	14:14:16.34	+53:35:08.39	2.453
7339-56799-0734	14:14:20.55	+53:22:16.67	2.217
7030-56448-0602	14:14:22.82	+52:51:20.63	2.149
7339-56722-0787	14:15:24.43	+53:28:32.77	2.153
7339-56799-0238	14:15:34.20	+52:57:43.22	2.061
7340-56837-0794	14:15:41.15	+53:51:04.20	2.420
7339-56768-0256	14:15:48.07	+52:09:09.94	2.469
7339-56799-0787	14:15:54.32	+53:53:57.02	2.191
7339-56722-0788	14:15:54.46	+53:17:06.92	2.138
7339-56799-0770	14:16:02.71	+53:17:45.03	2.207
6717-56397-0604	14:16:27.00	+53:19:40.10	2.428
7339-56799-0809	14:16:28.69	+53:31:00.40	2.273
7029-56455-0247	14:16:28.92	+52:03:29.00	2.134
7339-56722-0838	14:16:41.41	+53:21:47.17	2.214
7028-56449-0809	14:16:45.06	+53:05:10.15	2.529
7339-56772-0218	14:16:47.20	+52:11:15.26	2.158
7338-56745-0823	14:17:04.00	+53:38:07.47	2.501
7339-56799-0194	14:17:15.19	+53:03:03.76	2.164
7028-56449-0805	14:17:22.72	+52:58:51.62	2.405
7339-56751-0060	14:17:26.51	+52:18:56.51	2.151
7028-56449-0834	14:17:29.99	+53:38:25.69	2.119
7339-56722-0200	14:17:38.83	+52:23:33.07	2.153
7339-56722-0832	14:17:43.33	+53:11:45.67	2.059
7339-56799-0831	14:17:50.37	+53:45:17.76	2.177
7339-56772-0798	14:17:52.39	+53:48:49.43	2.093
7339-56799-0854	14:18:07.73	+53:17:54.02	2.278
7339-56722-0876	14:18:17.46	+53:11:16.82	2.232
7339-57518-0151	14:18:18.45	+52:43:56.05	2.136
7029-56455-0234	14:18:23.07	+52:41:18.81	2.050
7338-56745-0149	14:18:42.27	+52:36:43.97	2.128
7339-56772-0893	14:18:43.30	+53:19:20.83	2.301
7030-56448-0306	14:18:57.23	+52:18:23.39	2.167
7339-56772-0895	14:19:05.24	+53:53:54.17	2.427
7339-56799-0134	14:19:05.73	+52:12:38.07	2.219
7031-56449-0404	14:19:07.20	+52:01:51.74	2.172
7340-56825-0873	14:19:10.22	+53:47:07.11	2.373
7028-56449-0870	14:19:15.99	+53:49:24.13	2.209
7339-56772-0889	14:19:27.35	+53:37:27.70	2.368
7339-56772-0884	14:19:29.90	+53:35:01.41	2.390
7339-56799-0105	14:19:32.07	+52:26:39.46	2.162
7028-56449-0101	14:19:45.40	+52:23:33.57	2.378
7339-56799-0087	14:19:52.89	+52:01:16.87	2.229
7339-56799-0106	14:19:55.27	+52:27:41.19	2.141
7339-56722-0093	14:20:36.56	+52:14:55.05	2.212
7028-56449-0937	14:20:37.24	+52:58:51.00	2.274
7340-56837-0923	14:20:41.26	+53:33:55.30	2.421
7028-56449-0066	14:20:46.11	+52:24:21.61	2.256
7339-56799-0913	14:20:49.31	+53:52:11.59	2.221
7029-56455-0158	14:20:58.63	+52:40:44.43	2.489
7339-56772-0955	14:21:02.17	+53:39:44.14	2.292

Table 5. Foreground QSOs in the EGS field (continued)

ID	R.A. (J2000)	Decl. (J2000)	z_{spec}
7028-56449-0067	14:21:03.96	+52:37:12.53	2.235
7339-56722-0074	14:21:17.99	+52:53:46.00	2.308
7028-56449-0933	14:21:33.92	+53:02:45.52	2.150
7339-56722-0062	14:21:55.20	+52:27:49.48	2.516
7339-56799-0038	14:22:01.46	+52:32:50.26	2.121
7339-56799-0037	14:22:08.12	+52:29:08.65	2.370
7029-56455-0898	14:22:26.24	+52:57:09.93	2.095
7340-56726-0034	14:22:34.46	+52:58:38.02	2.138
7030-56448-0218	14:22:34.99	+52:00:10.05	2.109
7339-56772-0038	14:22:37.49	+52:53:35.86	2.226
7032-56471-0332	14:22:40.47	+52:04:11.81	2.267
7339-56780-0074	14:22:42.59	+52:44:15.69	2.171
7339-56772-0868	14:22:52.42	+53:36:48.86	2.084
7340-56837-0978	14:23:06.05	+53:15:29.03	2.468
7028-56449-0945	14:23:07.38	+53:34:39.84	2.074
7029-56455-0086	14:23:33.95	+52:07:00.95	2.271
7339-57481-0991	14:23:37.51	+53:18:28.89	2.435
7339-56799-0984	14:23:50.24	+53:29:29.31	2.136
7339-56799-0992	14:24:11.08	+53:20:41.38	2.362
7339-56772-0972	14:24:19.18	+53:17:50.62	2.530
7339-56768-0016	14:24:22.50	+52:59:03.22	2.138
7032-56471-0306	14:24:27.85	+52:20:44.40	2.331
7029-56455-0032	14:24:32.08	+52:22:20.49	2.194
7031-56449-0346	14:24:38.98	+52:21:39.15	2.259
7031-56449-0655	14:24:48.10	+53:21:21.42	2.066
7030-56448-0159	14:25:06.97	+52:54:44.33	2.546
7032-56471-0723	14:25:23.43	+53:29:45.88	2.182
7032-56471-0298	14:25:51.03	+52:05:09.06	2.315

spectra with estimated continua to create input spectra for H I tomography (Section 3.1.1) and 2) reconstructing the H I LSSs from the normalized spectra (Section 3.1.2).

3.1.1. Intrinsic Continua

To probe H I absorption along the lines of sight to the background QSOs, we estimate the Ly α forest transmission in the 1041–1185 Å rest frame,

$$F(z) = f_{\text{obs}}/f_{\text{int}}, \quad (1)$$

where f_{obs} is the observed continuum flux density and f_{int} is the intrinsic continuum flux density that is not affected by the Ly α forest absorption due to the IGM. We estimate f_{int} of our background QSOs, applying the continuum fitting technique of the mean-flux regulated/principal component analysis (MF-PCA; Lee et al. 2012) with the code developed by Lee et al. (2013; see also Lee et al. 2014b). In this technique, there are two steps. The first step is to fit spectral templates of QSOs to the observed spectra redward of Ly α to obtain initial estimates of the continuum spectra blueward of Ly α . In the same manner as Lee et al. (2014b), we use the spectral templates of QSOs constructed by Suzuki et al.

Our H I tomography analysis consists of the following two processes: 1) normalizing the background source

Table 6. Background QSOs in the EGS field

ID	R.A. (J2000)	Decl. (J2000)	z_{spec}	g (AB)
7339-56799-0270	14:14:08.64	+52:40:38.64	2.790	20.59
7339-56722-0800	14:14:18.24	+53:50:46.68	2.729	21.43
7339-56799-0734	14:14:20.64	+53:22:16.68	2.212	19.54
7339-56799-0730	14:14:35.52	+53:25:36.84	2.861	20.72
7339-56722-0297	14:14:39.12	+52:06:16.20	2.914	20.93
7339-56799-0728	14:14:44.16	+53:35:55.68	2.734	21.55
7339-56799-0277	14:15:08.64	+53:00:19.80	2.765	21.36
7340-56837-0794	14:15:41.04	+53:51:04.32	2.420	20.81
7027-56448-0068	14:15:51.36	+52:27:40.68	2.583	19.86
7028-56449-0809	14:16:45.12	+53:05:10.32	2.529	21.68
7339-56772-0218	14:16:47.28	+52:11:15.36	2.153	18.70
7340-56837-0833	14:17:22.32	+53:48:52.92	2.726	20.71
7339-56799-0831	14:17:50.40	+53:45:17.64	2.190	20.30
7339-56799-0854	14:18:07.68	+53:17:53.88	2.274	20.67
7339-56722-0876	14:18:17.52	+53:11:16.80	2.238	20.50
7339-56772-0893	14:18:43.20	+53:19:21.00	2.298	20.56
7340-56837-0117	14:19:12.48	+52:08:17.88	2.563	19.78
7339-56799-0087	14:19:52.80	+52:01:17.04	2.224	19.48
7339-56772-0924	14:20:10.56	+53:12:23.76	2.597	20.09
7027-56448-0994	14:20:33.12	+53:07:35.04	2.880	21.55
7340-56837-0923	14:20:41.28	+53:33:55.44	2.421	20.87
7339-56799-0074	14:21:13.20	+52:49:30.00	2.644	19.36
7339-56722-0074	14:21:18.00	+52:53:45.96	2.306	19.95
7339-56799-0069	14:21:38.64	+52:33:24.48	2.606	20.30
7339-56799-0068	14:21:41.28	+52:45:51.84	2.654	21.04
7339-56722-0062	14:21:55.20	+52:27:49.32	2.516	21.10
7339-56768-0038	14:22:39.60	+52:28:52.68	2.989	21.61
7339-56780-0074	14:22:42.48	+52:44:15.72	2.175	20.03
7340-56837-0978	14:23:06.00	+53:15:29.16	2.468	18.29
7029-56455-0100	14:23:17.28	+52:13:12.72	2.671	21.54
7032-56471-0340	14:23:37.20	+52:16:07.68	2.894	19.73
7339-56799-0992	14:24:11.04	+53:20:41.28	2.366	20.31
6710-56416-0442	14:24:11.52	+53:50:26.88	2.769	20.96
7339-56799-0014	14:24:18.24	+53:04:06.60	2.859	19.56
7339-56772-0972	14:24:19.20	+53:17:50.64	2.530	20.49
7032-56471-0306	14:24:27.84	+52:20:44.52	2.324	20.03
7029-56455-0955	14:24:33.12	+53:43:52.68	2.711	20.51
7030-56448-0160	14:24:50.88	+52:50:01.68	2.728	19.71
7030-56448-0130	14:24:55.68	+52:06:09.72	2.631	21.20
7031-56449-0356	14:24:58.56	+52:41:49.92	3.015	21.27
7031-56449-0334	14:25:06.24	+52:01:28.92	2.736	21.92
6710-56416-0446	14:25:09.12	+53:51:49.32	3.102	21.37
7032-56471-0729	14:25:10.80	+53:23:09.60	2.861	20.73

(2005). The second step is to constrain the amplitude and slope of the blueward spectra that should match to previous measurements of the cosmic mean $\text{Ly}\alpha$ forest transmission, $F_{\text{cos}}(z)$. We adopt $F_{\text{cos}}(z)$ estimated by Faucher-Giguère et al. (2008),

$$F_{\text{cos}}(z) = \exp[-0.00185(1+z)^{3.92}]. \quad (2)$$

With F_{cos} we estimate f_{int} (Figure 5), and use Equation (1) to obtain $F(z)$. Note that the strong stellar and interstellar absorptions of $\text{NII } \lambda 1084$ and $\text{CIII } \lambda 1175$ associated with the QSO host galaxies in the $\text{Ly}\alpha$ forest wavelength range could bias the results. For conservative estimates, we do not use the spectra in the wavelength ranges of $\pm 5\text{\AA}$ around these lines in our analyses. The uncertainties of $F(z)$ are calculated from the errors of the f_{obs} measurements and the f_{int} estimates based on the MF-PCA continuum fitting, the latter of which are evaluated by Lee et al. (2012) as a function of redshift and median S/N over the $\text{Ly}\alpha$ forest wavelength range (see Figure 8 of Lee et al. 2012). Specifically, we adopt MF-PCA continuum fitting errors of 7%, 6%, and 4% for spectra with median S/Ns over the $\text{Ly}\alpha$ forest wavelength ranges of 2–4, 4–10, and > 10 , respectively.

Based on the estimated $F(z)$ and the cosmic mean $\text{Ly}\alpha$ forest transmission $F_{\text{cos}}(z)$, we calculate the $\text{Ly}\alpha$ forest fluctuation (hereafter referred to as HI transmission overdensity) δ_F for our background QSOs,

$$\delta_F = \frac{F(z)}{F_{\text{cos}}(z)} - 1, \quad (3)$$

where negative values correspond to strong HI absorptions. The errors of δ_F are calculated with the uncertainties of $F(z)$. We confirm that the systematic effect of using different prescriptions of $F_{\text{cos}}(z)$ obtained by Becker et al. (2013) and Inoue et al. (2014) is minor, only within 2%, which is not as large as the uncertainties of $F(z)$.

3.1.2. Reconstruction Processes

Once we obtain the δ_F spectra of the background QSOs, we carry out HI tomographic reconstruction to reveal the 3D distribution of the HI gas. In the same manner as Lee et al. (2018, 2016, 2014b), we use the reconstruction code developed by Stark et al. (2015).⁴ The reconstruction code performs Wiener filtering for the estimated δ_F values along the sightlines of our background QSOs. The Wiener filtering is based on the following two calculations: the first is Gaussian smoothing with the scale of the mean transverse sightline separation $\langle d_{\perp} \rangle$, which determines the spatial resolution of the tomography map; the second is input pixel weighting by the S/N to remove possible systematics caused by low S/N spectra.

Specifically, in the Wiener filtering, the reconstructed HI transmission overdensity map δ_F^{rec} is given by the following estimator (Stark et al. 2015; Lee et al. 2014a; Caucci et al. 2008; Pichon et al. 2001),

$$\delta_F^{\text{rec}} = \mathbf{C}_{\text{MD}} \cdot (\mathbf{C}_{\text{DD}} + \mathbf{N})^{-1} \cdot \delta_F^{\text{obs}}, \quad (4)$$

where δ_F^{obs} is the input HI transmission overdensity datacube comprised of our background source spectra and

⁴ <https://github.com/caseywstark/dachshund>

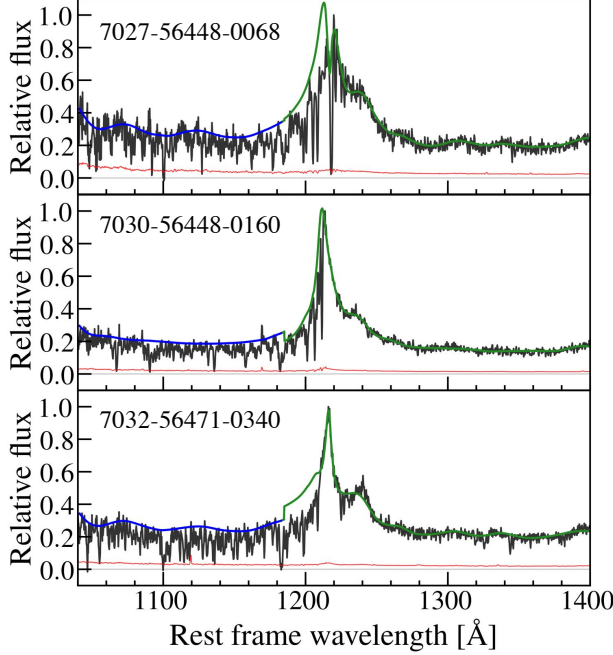


Figure 5. Example spectra of our background QSOs. The black (red) lines depict flux (error) per pixel. The grey lines show zero flux level. The green curves are the Suzuki et al. (2005) template overplotted at the source redshifts. The blue curves are the Suzuki et al. (2005) template representing the estimated continua.

coordinates. \mathbf{C}_{MD} , \mathbf{C}_{DD} , and \mathbf{N} are the map-datacube, datacube-datacube, and noise covariances, respectively. The estimator, $\mathbf{C}_{\text{MD}} \cdot (\mathbf{C}_{\text{DD}} + \mathbf{N})^{-1}$, is constructed so that it minimizes an expected error between the reconstructed δ_F^{rec} and the actual HI distribution (Stark et al. 2015, and references therein). The estimator also allows us to down-weight pixels in low S/N spectra. These covariances are assumed to be a Gaussian covariance between any two points \mathbf{r}_1 and \mathbf{r}_2 .

$$\mathbf{C}_{\text{DD}} = \mathbf{C}_{\text{MD}} = \mathbf{C}(\mathbf{r}_1, \mathbf{r}_2) \quad (5)$$

and

$$\mathbf{C}(\mathbf{r}_1, \mathbf{r}_2) = \sigma_F^2 \exp \left[-\frac{(\Delta r_{\parallel})^2}{2L_{\parallel}^2} \right] \exp \left[-\frac{(\Delta r_{\perp})^2}{2L_{\perp}^2} \right], \quad (6)$$

where Δr_{\parallel} and Δr_{\perp} (L_{\parallel} and L_{\perp}) are the line-of-sight (LOS) and transverse distances between \mathbf{r}_1 and \mathbf{r}_2 (correlation lengths), respectively. We adopt $L_{\parallel} = L_{\perp} = \langle d_{\perp} \rangle$ as well as a normalization of $\sigma_F^2 = 0.05$ in the same manner as Lee et al. (2018, 2014b). More details about the reconstruction process is presented in Stark et al. (2015) and Lee et al. (2018).

3.2. HI Tomography Maps

In the COSMOS field, we use the HI tomography map of Lee et al. (2018) (Section 3.2.1), while in the EGS field we make the HI tomography map with the δ_F spectra of our background QSOs (Section 3.2.2).

3.2.1. COSMOS

For the COSMOS field, we use the public data of the COSMOS HI tomography map made by the CLAMATO survey (Lee et al. 2018)⁵. The COSMOS HI tomography map is a 3D map of the IGM HI absorption at $z = 2.05$ – 2.55 in a 0.157 deg^2 area of the COSMOS field, having a $30 \times 24 \times 444 \text{ h}^{-3} \text{ cMpc}^3$ cosmic volume with a spatial resolution of $2.5 \text{ h}^{-1} \text{ cMpc}$ and a grid size of $0.5 \text{ h}^{-1} \text{ cMpc}$. The HI tomography map is reconstructed from the spectra of 240 background galaxies and QSOs at $z = 2.2$ – 3.0 . The sky distribution of these background sources is shown in Figure 1. Figures 6 and 7 present the COSMOS HI tomography map and the δ_F pixel distribution, respectively. For error estimates in Section 4.1, we generate 1000 mock HI tomography maps to which we give random perturbations following the Gaussian distribution with sigma defined by the data values of the error map, where the error map is estimated from the 1σ uncertainties of δ_F spectra of the background sources in the CLAMATO survey (Lee et al. 2018). The typical 1σ uncertainty of δ_F for a pixel in the HI tomographic map is found to be about 0.1.

3.2.2. EGS

For the EGS field, we conduct large-scale HI tomography mapping with our background QSOs (Figure 2). The mean transverse sightline separation is $\langle d_{\perp} \rangle = 20 \text{ h}^{-1} \text{ cMpc}$ which is about ten times larger than those of the background sources in the COSMOS field (Section 3.2.1). We aim to complement the COSMOS-field HI tomography with the EGS-field HI tomography that covers a large volume, albeit with coarse resolution. For our tomographic reconstruction, we choose a redshift range of $z = 2.05$ – 2.55 that is the same as the one of the COSMOS HI tomography map (Lee et al. 2018, Section 3.2.1). This redshift range and the 6.0 deg^2 sky area of the EGS field give an overall cosmic volume of $124 \times 136 \times 444 \text{ h}^{-3} \text{ cMpc}^3$. We adopt a grid size of $1.0 \text{ h}^{-1} \text{ cMpc}$ that over-samples the spatial resolution of $20 \text{ h}^{-1} \text{ cMpc}$. Figures 8 and 9 present the EGS HI tomography map and the δ_F pixel distribution, respectively. For error estimates, we create mock Ly α forest transmission data $F(z)$ for the 43 background sightlines, adding Gaussian-distribution random noise based on the uncertainties of $F(z)$ that are obtained in Section 3.1.1. We then perform HI tomography mapping with the mock data. Repeating this process to produce 100 mock HI tomography maps, with the total limited by computing resources. The typical 1σ uncertainty of δ_F

⁵ <https://clamato.lbl.gov/>

for a pixel in the HI tomographic map is found to be about 0.1.

One might expect that the HI-gas distribution in the EGS HI tomography map could be affected by interpolation in the tomographic reconstruction process, due to the coarse distribution of sightlines. Recently, [Ravoux et al. \(2020\)](#) have simulated large-scale HI tomography of eBOSS background QSOs whose sightline separation is $\simeq 15 h^{-1}$ cMpc, and demonstrated that the correlation of the reconstructed HI-gas distribution and the underlying matter field is retained on large-scales. The correlation of HI-gas and underlying matter is also investigated by [Cai et al. \(2016\)](#) and a strong correlation is suggested on $15 - 25 h^{-1}$ cMpc scales⁶. The simulation study of [Ozbek et al. \(2016\)](#) assessed the statistical properties of large-scale HI tomography based on eBOSS background QSOs. They estimated the root-mean-square error for a δ_F pixel reconstructed with $\simeq 20 h^{-1}$ cMpc resolution is $\simeq 0.02$ which is smaller than the δ_F pixel error of the EGS HI tomography map.

4. RESULTS

In this section, we investigate the IGM HI-gas distributions around $z \sim 2$ galaxies in our two HI tomography maps.

4.1. Spatial Correlations Between HI Gas and Galaxies

We present the results of spatial correlations between IGM HI gas and galaxies in the COSMOS blank field. The results consist of two components: a 2D distribution map of δ_F as a function of distance and a radial profile of δ_F (hereafter HI radial profiles) as a function of distance.

We measure δ_F around the 27 LAEs (Section 2.1) in our COSMOS HI tomography map (Section 3.2.1) along the transverse D and the line-of-sight (LOS) Z directions. The comoving distances of D and Z are computed under the assumption of Hubble flow. We take the average of HI tomography pixel arrays over a distance $\pm Z/2 h^{-1}$ cMpc along the LOS direction at a fixed distance $D h^{-1}$ cMpc in the transverse direction from LAEs. Here we use $\text{Ly}\alpha$ redshifts for the redshifts of LAEs. We estimate 1σ errors of the averaged δ_F , calculating standard deviations of the measurements with the 1000 mock tomography maps (Section 3.2.1).

Figure 10 shows the 2D HI distribution map of the COSMOS LAEs. In Figure 10, the LAEs are located at $(Z, D) = (0, 0) h^{-1}$ cMpc. There exist HI absorption enhancements around LAEs at $-7 \lesssim Z \lesssim 3 h^{-1}$ cMpc along the LOS direction and $D \lesssim 8 h^{-1}$ cMpc in the transverse direction from the LAEs. The HI absorption enhancements have an anisotropic distribution whose HI absorption peak has an offset toward the observer by

$\sim 2 h^{-1}$ cMpc corresponding to the blueshift of $\sim 200 \text{ km s}^{-1}$ from the LAE $\text{Ly}\alpha$ redshifts. This blueshift is consistent with the recent MUSE galaxy-background QSO pair study of [Muzahid et al. \(2019\)](#), and is explained by a well-known velocity offset of a $\text{Ly}\alpha$ redshift from a galaxy systemic redshift by $\sim 200 \text{ km s}^{-1}$ for LAEs on average ([Steidel et al. 2010](#); [Hashimoto et al. 2013](#); [Shibuya et al. 2014](#); [Song et al. 2014](#); see [Ouchi et al. 2020](#) in press and references therein) due to $\text{Ly}\alpha$ resonant scattering (e.g., [Neufeld 1990](#); [Dijkstra et al. 2006](#)). In other words, our 2D HI distribution map reproduces the average $\sim 200 \text{ km s}^{-1}$ offset of $\text{Ly}\alpha$ redshifts by the independent analysis that is different from previous studies requiring both galaxy $\text{Ly}\alpha$ and systemic redshift determinations from other spectral features.

Figure 10 also shows an elongated HI-gas distribution whose absorption enhancements are stronger in the transverse direction than along the LOS direction from the HI absorption peak. This elongation may originate from large-scale gas infall toward the galaxy halos as claimed in previous galaxy-background QSO pair studies ([Turner et al. 2014](#); [Bielby et al. 2017](#)) and as predicted by numerical simulations ([Turner et al. 2017](#); [Kakiichi & Dijkstra 2018](#)). A detailed analysis with radiative transfer simulations for the elongated HI-gas distribution will be presented in a forthcoming publication ([Byrohl et al. in preparation](#)).

We measure HI radial profiles around the COSMOS LAEs (Section 2.1), spherically averaging radial profiles of δ_F taken from the COSMOS HI tomography map (Section 3.2.1) as a function of 3D distance from the LAEs. This is the similar analysis of HI-QSO performed in a previous study of [Mukae et al. \(2020\)](#). The 3D distances from the LAEs are defined as

$$R_{3D} \equiv \sqrt{D^2 + d_z^2}, \quad (7)$$

where d_z is the Hubble flow comoving distance from the LAEs under the assumption that the HI absorbers have zero peculiar velocities relative to the LAEs. To estimate uncertainties of the spherically averaged δ_F , we use the 1000 mock HI tomography maps (Section 3.2.1). For each mock map, we compute HI radial profiles averaged over our LAEs, to obtain 68% intervals as 1σ confidence intervals.

In Figure 11, the black circles present the average HI radial profile of the COSMOS LAEs. The value of δ_F decreases (i.e., the HI absorption increases) from the cosmic mean level $\delta_F = 0$ to -0.1 with decreasing R_{3D} from $\sim 10 h^{-1}$ cMpc to $\sim 1 h^{-1}$ cMpc around the LAEs. In other words, our HI radial profile shows strong HI absorption exists around galaxies up to the $10 h^{-1}$ cMpc scale. This trend is consistent with the one found for bright LAEs by [Momose et al. \(2020\)](#), whose $\text{Ly}\alpha$ luminosity limit for the bright LAEs is $L_{\text{Ly}\alpha} \geq 10^{43} \text{ erg s}^{-1}$, comparable to the $\text{Ly}\alpha$ luminosity limit of the HETDEX LAEs (Section 2.1).

⁶ It is noted that the HI-gas distribution on a few Mpc scales can be affected by the strong ionizing radiation of the QSOs ([Mukae et al. 2020](#); [Momose et al. 2020](#))

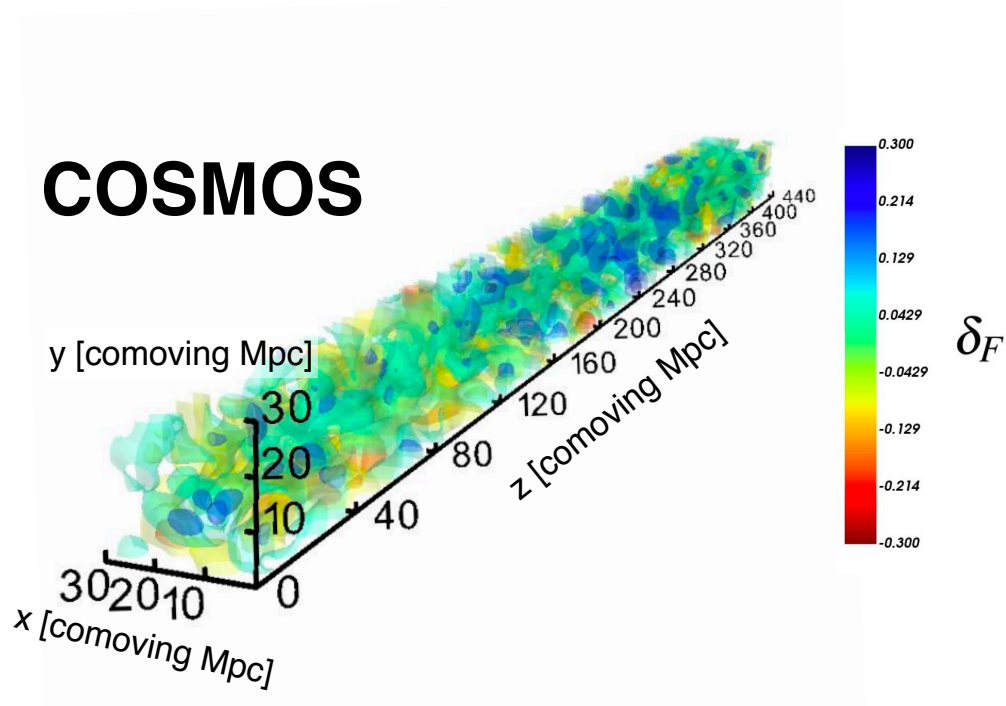


Figure 6. COSMOS Hi tomography map reconstructed from HI absorption in the spectra of the background galaxies and QSOs (Lee et al. 2018). The spatial axes of R.A., Decl., and z (Hubble flow distances) correspond to the x , y , and z axes, respectively, that are shown in comoving scale. The redshift range of the HI tomography map is $z = 2.05$ – 2.55 . The color contours represent the HI transmission overdensity δ_F whose negative values (in red color) correspond to high HI overdensities. The δ_F 's maximum (minimum) scale of this figure is set to $+0.3$ (-0.3) for visualization. The δ_F values of some volumes do not fall in the range of $-0.3 < \delta_F < 0.3$, but all are in $-0.5 < \delta_F < 0.5$. The cosmic large-scale structures are roughly traced by the HI transmission overdensities.

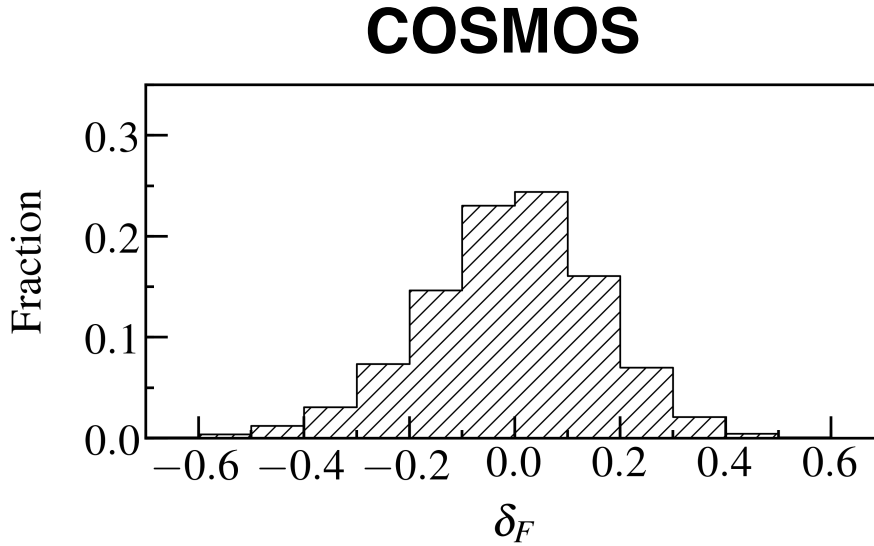


Figure 7. Histogram of the δ_F pixel distribution of the COSMOS Hi tomography map.

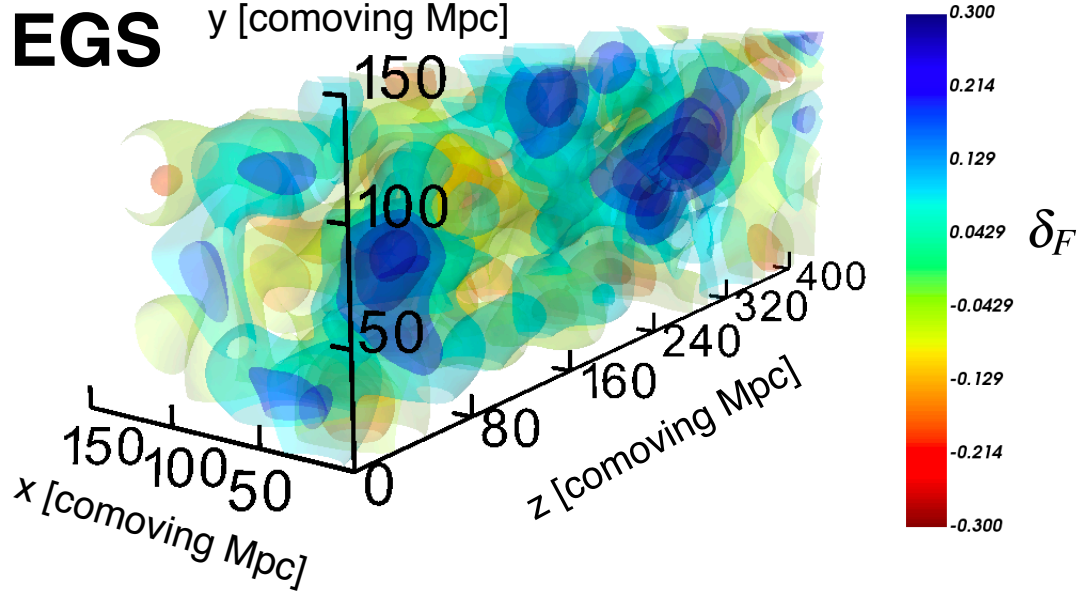


Figure 8. Same as Figure 6, but for the EGS HI tomography map. Note that the spatial resolution is $20 h^{-1} \text{ cMpc}$ which is larger than the one of COSMOS ($2.5 h^{-1} \text{ cMpc}$). The δ_F values of some volumes do not fall in the range of $-0.3 < \delta_F < 0.3$, but all are in $-0.6 < \delta_F < 0.6$. This HI tomography map does not have a spatial resolution as high as the one of Figure 6, but covers a cosmic volume larger than that of Figure 6.

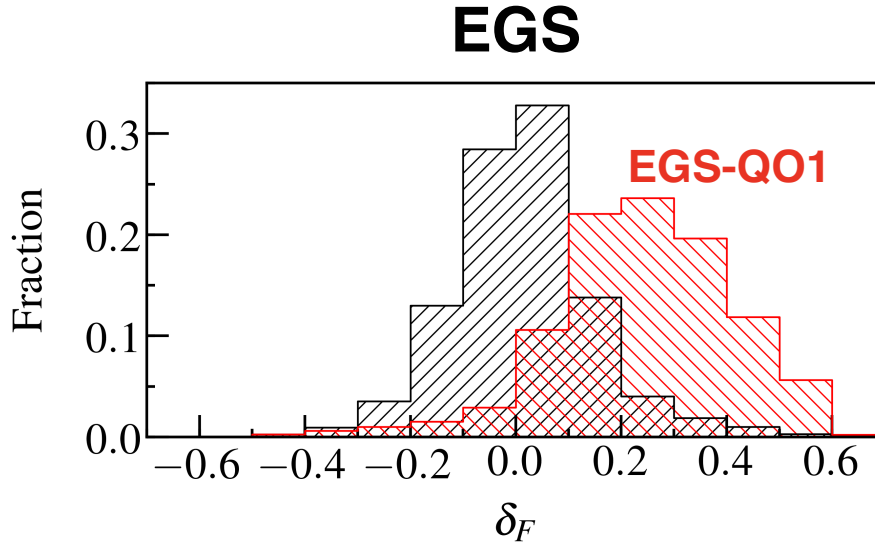


Figure 9. Same as Figure 7, but for the EGS HI tomography map. The red histogram presents the δ_F pixel distribution of the QSO overdensity EGS-Q01 (Section 4.2).

All of the results of the two components above indicate HI absorption excesses around galaxies over Mpc scales (consistent with those of previous galaxy-background QSO pair studies of Turner et al. (2017), Bielby et al. (2017)), which confirm the impression of a spatial correlation between HI and galaxies seen in Figure 12. Note that these results of the spatial correlations are free from influences of bright type-I QSOs, because no eBOSS QSOs at $z = 2.05\text{--}2.55$ are found in the cosmic volume of the COSMOS HI tomography map (Section 2.2.1).

4.2. HI-Gas Distribution Around an Extreme QSO Overdensity

We investigate the IGM HI-gas distribution around QSOs and galaxies in an extreme QSO overdensity.

First, we search for QSO overdensities in the large 6.0-deg^2 area of the EGS field that is sufficient to find rare systems of QSO overdensities (e.g., Cai et al. 2017; Hennawi et al. 2015). We use the 78 foreground QSOs (Section 2.2.1), and estimate QSO overdensities within a sphere of radius $20 h^{-1}$ cMpc at $z = 2.3$. This radius is larger than the one applied for galaxy overdensity measurements (Chiang et al. 2013, 2014), because the number density of QSOs is about two orders of magnitude smaller than that of galaxies at $z \sim 2$. The QSO overdensity is defined as

$$\delta_{\text{QSO}} \equiv \frac{n_{\text{QSO}}}{\bar{n}_{\text{QSO}}} - 1, \quad (8)$$

where n_{QSO} (\bar{n}_{QSO}) is the number density (mean number density) of the QSOs in a sphere. The mean number density is derived in the cosmic volume of the HI tomography map. The expected number of QSOs in the sphere is about 0.35 comparable to that estimated from QSO luminosity functions (e.g., Palanque-Delabrouille et al. 2013) integrated to the detection limit of the eBOSS QSOs ($g \simeq 22$ mag). We calculate δ_{QSO} at pixel positions of the EGS HI tomography map, and make a δ_{QSO} map whose volume coverage is similar to that of the HI tomography map. Searching for the largest QSO overdensity in the δ_{QSO} map, we find an extremely high overdensity at $z = 2$, dubbed EGS-QO1, whose QSO overdensity is $\delta_{\text{QSO}} = 16.2 \pm 7.0$. The top panel of Figure 13 shows a projection of a $40 h^{-1}$ cMpc-width slice of our δ_{QSO} map with EGS-QO1. The overdensity of EGS-QO1 is clearly distinguished.

Next, we inspect the HI environment of EGS-QO1 with the HI tomography map. The bottom panel of Figure 13 shows the projected HI tomography map of the same slice as presented in the top panel of Figure 13. Comparing the top and bottom panels of Figure 13, we find that EGS-QO1 resides in an HI underdensity volume with a size of $\sim 40 \times 70 \times 40 h^{-3}\text{cMpc}^3$ at $z = 2.13\text{--}2.19$ (centered at $\langle z \rangle = 2.16$). Red histogram in Figure 9 depicts the δ_F pixel distribution of EGS-QO1. The HI absorption values in EGS-QO1 ranges $\delta_F \simeq 0.1\text{--}0.4$, indicating that the EGS-QO1 resides

in an HI underdensity volume. Note that the typical 1σ uncertainty of δ_F for a pixel in the HI tomographic map is 0.1 (Section 3.2.2). Although no background QSOs probe HI absorption at the exact sky center of the HI underdensity volume, spectra of several of the QSOs distributed over this volume show evidence of the HI underdensity (Figure 14). The HI underdensity associated with the QSO overdensity suggests that the QSOs forming the EGS-QO1 overdensity would make a large ionized bubble, where the HI gas is widely photoionized by the strong ionizing radiation of the QSOs.

The ionized bubble may be created by overlap of proximity zones of the QSOs, each of which should have a typical size of $\sim 10\text{--}15 h^{-1}$ cMpc in diameter at $z \sim 2$ (e.g., D’Odorico et al. 2008; Mukae et al. 2020; Jalan et al. 2019). If the ionized bubble length of $\sim 40 h^{-1}$ cMpc is made by three QSOs roughly distributed along the redshift direction in EGS-QO1, each QSO would form a proximity zone with $40/3 \simeq 13 h^{-1}$ cMpc in diameter, which is comparable to typical sizes in the literature. When the proximity zone size is simply divided by the speed of light, we obtain QSO lifetimes of $t_{\text{QSO}} = 10^{7.3}$ years consistent with typical values of $t_{\text{QSO}} = 10^{7-9}$ years that are constrained by clustering measurements (e.g., Adelberger & Steidel 2005; White et al. 2012; Conroy & White 2013).

Note that the HI absorption is made by the ionized IGM with HI fraction as low as $\sim 0.6 \times 10^{-6}$ ⁷. Even outside of the ionized bubble, the IGM is highly ionized with the cosmic average HI fraction of $\sim 2.0 \times 10^{-6}$ at $z = 2$ (McQuinn 2016). The ionized bubble defined here is the cosmic volume with small HI fraction that is probably caused by the strong QSO radiation.

We then measure the HI radial profile averaged over the six QSOs forming the EGS-QO1 overdensity. Figure 15 represents the average HI radial profile around the six QSOs. The δ_F values increase (i.e., HI absorption weakens) from the cosmic mean level ($\delta_F = 0$) to $\delta_F = 0.1$ with decreasing R_{3D} from $\sim 100 h^{-1}$ cMpc to $\sim 10 h^{-1}$ cMpc around the QSOs. This HI radial profile suggests strongly-suppressed HI absorption around the QSOs in the extreme QSO overdensity. It is a clear contrast with the results of the blank fields; the HI radial profile of the rest of 72 QSOs that reside outside of the EGS-QO1 (here after referred to as EGS outside; Figure 15) and the HI radial profile of galaxies in the COSMOS field (Figure 11).

Here we need to examine whether this contrast is made by the choices of the HI radial profile measure-

⁷ The HI fraction is obtained with a ratio of the EGS-QO1 value to the cosmic value at $z = 2$ (McQuinn 2016). The ratio is simply estimated from a ratio of column densities that are converted from optical depth of $\delta_F \simeq 0.2$ (the peak value of the δ_F fraction in Figure 9) and $\delta_F = 0.0$ (the cosmic mean value) under the assumption of optically-thin Ly α forest clouds (Draine 2011; Mo et al. 2010).

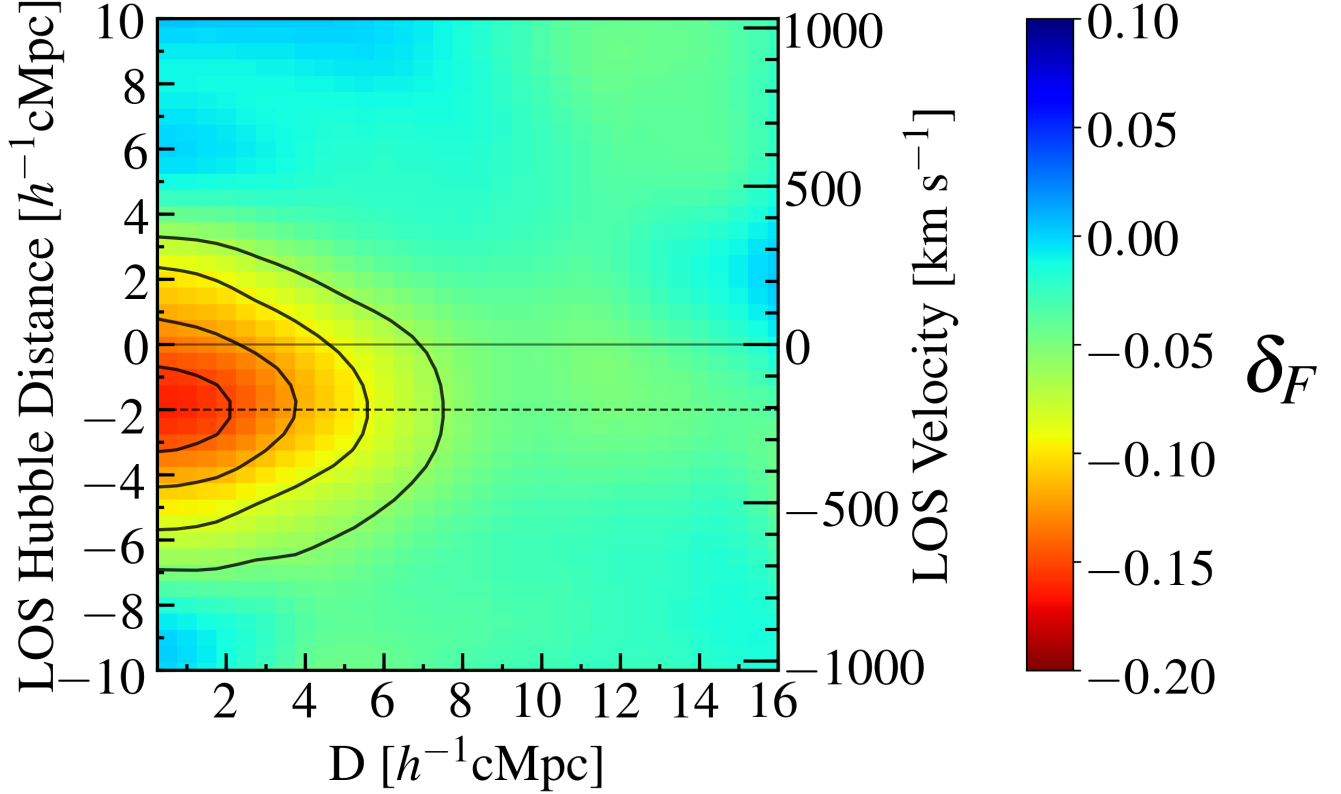


Figure 10. Averaged 2D HI absorption map as a function of transverse D and LOS Hubble distances from our LAEs in the COSMOS field. The bin size is $0.5 h^{-1} \text{cMpc}$ and the map is smoothed by a 2D Gaussian kernel with a FWHM of $1.5 h^{-1} \text{cMpc}$. The color code represents the HI transmission overdensity δ_F . The black contours indicate the significance levels of the δ_F values (over the errors) from the 2 to 5 σ levels by a step of 1σ . The apparent HI transmission overdensity is centered at -2 in the LOS Hubble distance (200 km s^{-1} blueshift) due to $\text{Ly}\alpha$ radiative transfer.

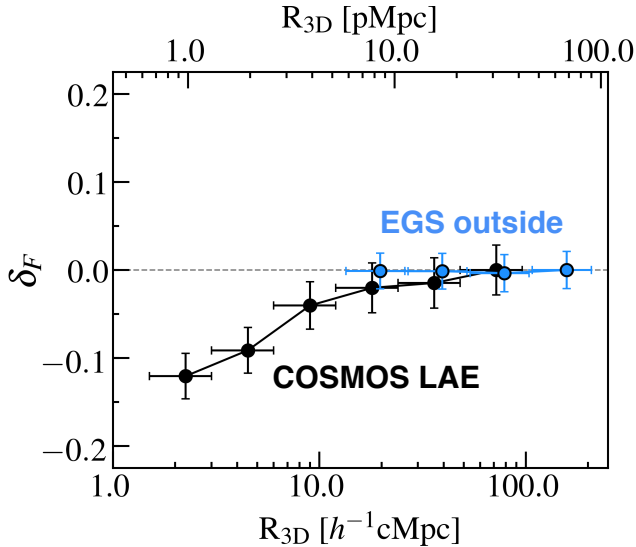


Figure 11. HI radial profile around LAEs in the blank fields. The black circles are the COSMOS LAEs (Section 4.1). The blue circles are the EGS LAEs that reside outside of the QSO overdensity EGS-QO1 (i.e. EGS outside; Section 4.2). The horizontal bars represent the measurement boundaries for the average. The gray dashed line is the cosmic mean level of the IGM HI absorption at $z = 2.3$. A modest HI transmission overdensity is found near LAEs.

ment centers (QSOs vs. galaxies) or the environment (QSO overdensity vs. blank field). In the cosmic volume of the EGS HI tomography map, we find 26 LAEs, four of which reside in the EGS-QO1 QSO overdensity at $z = 2.13\text{--}2.19$. These four LAEs, dubbed LAE1-4 are shown with black circles and white labels in Figure 13. In EGS-QO1, the density of LAEs is high, and there is a moderate LAE overdensity of ~ 1 in a radius of $20 h^{-1}$ cMpc. Figure 16 presents the HETDEX spectra and CFHT/HST images of LAE1-4. We calculate HI radial profiles around LAE1-4 in the EGS-QO1 QSO overdensity in the same manner as Section 4.1, and show the average HI radial profile in Figure 17. We find that this HI radial profile around the LAEs (Figure 17) is similar to that of the QSOs in EGS-QO1 (Figure 15) and clearly different from the one around LAEs in the blank field (Figure 11). We also measure the HI radial profiles around the rest of 22 LAEs that reside outside of EGS-QO1 (i.e. EGS outside; Figure 11), and find that the HI radial profile is consistent with the one in the blank field on the scale down to $\sim 20 h^{-1}$ cMpc the resolution limit of the EGS HI tomography map. In other words, the HI absorption is significantly weakened around galaxies in the QSO overdensity EGS-QO1, in contrast with the strong HI absorption around galaxies in the blank field (Section 4.1). The weak HI absorption around galaxies found in EGS-QO1 is probably caused by the environ-

ment of the QSO overdensity that produces the ionized bubble.

We find that one of the four LAEs, LAE4, shows triple-continuum components over the scale of a 10 pkpc-radius circle on the HST F814W/F160W images of the EGS, indicative of a triple merging system (middle/bottom panels of Figure 18). LAE4 is located at (R.A., Decl.)=(14:19:13.02, +52:49:11.2) near the center of the ionized bubble of EGS-QO1 (bottom panel of Figure 13). The average Ly α redshift of LAE4 over the HETDEX fibers is $z_{\text{Ly}\alpha} = 2.156$, and the total Ly α luminosity over the fibers is $L_{\text{Ly}\alpha}^* = 10^{43.06}$ erg s $^{-1}$. The top panel of Figure 18 presents the spectrum of LAE4, summed over the fibers, which is the same as the one in Figure 16. The spectrum of LAE4 has a broad Ly α emission line whose FWHM is ~ 1100 km s $^{-1}$ (about 3 times broader than the instrumental resolution), possibly suggesting a type-I AGN (e.g. Kakuma et al. in preparation)⁸. The bottom panel of Figure 18 presents the positions and the sky coverage of the fibers used for the measurements of the LAE4 Ly α redshift and total luminosity, and indicates three fibers cover the triple-continuum components with the blue, green, and yellow circles. The spectra of these three fibers are shown on the right-hand side in Figure 18. All of the three fiber spectra of the blue, green, and yellow circles have Ly α emission lines at $z_{\text{Ly}\alpha} = 2.16$, suggesting that the three objects probably reside at the same redshift. Moreover, these three fiber spectra have broad Ly α emission lines with an FWHM of ~ 1000 km s $^{-1}$. Although each of these fibers does not separately cover one of the triple-continuum components whose blending due to the HET image quality and large fiber diameter may produce apparent broad lines, these broad Ly α emission lines found in the different positions over the triple-continuum components imply that the LAE4 system could be a merging type-I AGN doublet or triplet.

5. DISCUSSION

In Section 4.1, we have investigated spatial correlations between IGM HI-gas and galaxies in the COSMOS field, the blank field with no QSO overdensities. We have found that strong HI absorption exists around galaxies up to the $10 h^{-1}$ cMpc scale. The result suggests a picture where a galaxy resides in an HI-gas overdensity in a blank field as illustrated in Figure 19 (a).

In Section 4.2, we have studied spatial correlations between IGM HI-gas and galaxies in the EGS field, where the extreme QSO overdensity EGS-QO1 of six QSOs is found. There is also a galaxy overdensity in EGS-QO1, traced by LAEs. In the HI tomography map of the EGS field, EGS-QO1 resides in an ionized bubble with a size

⁸ Other AGN features of high-ionization emission lines, CIV $\lambda 1549$ Å and HeII $\lambda 1640$ Å, are not detected in the LAE4 spectrum shown in Figure 16. This is probably because the LAE4 is optically faint (~ 25 mag) and its metal lines are too faint to be identified.

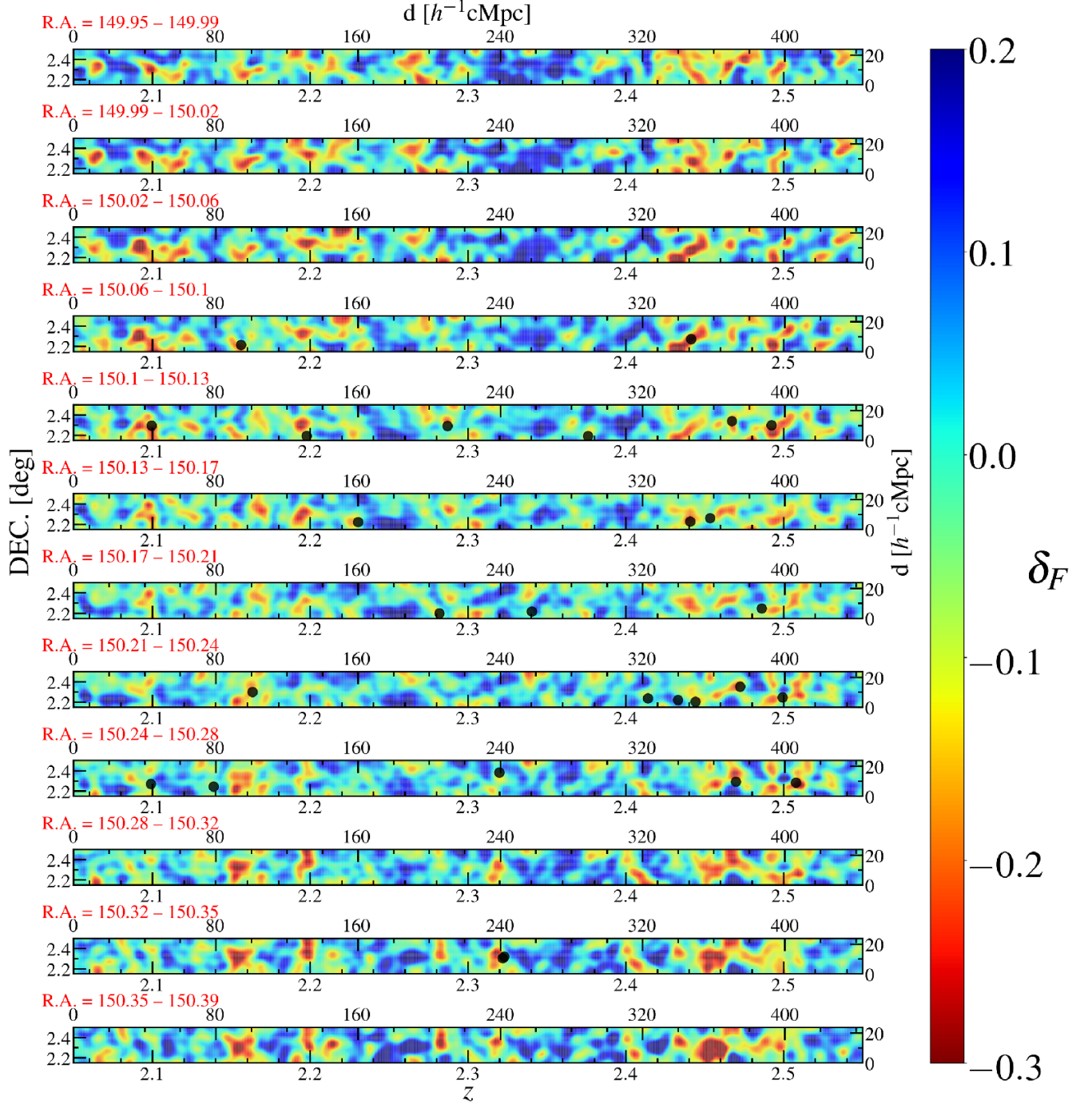


Figure 12. Projections of 2.5 h^{-1} cMpc-width slices of the HI tomography map in COSMOS over the R.A. direction. The width of the slice is comparable to the spatial resolution of the HI tomography map (Section 3.2.1). The color contours represent the HI transmission overdensity δ_F : the red (blue) color denotes a negative (positive) δ_F value that corresponds to a strong (weak) HI absorption. The black dots indicate positions of the COSMOS LAEs. Because there are no eBOSS QSOs in this small volume of the COSMOS HI tomography map, no QSOs are shown in this figure. Visual inspection may find potential spatial correlations between HI absorption and LAEs, but quantitative analysis is needed to quantify the spatial correlations.

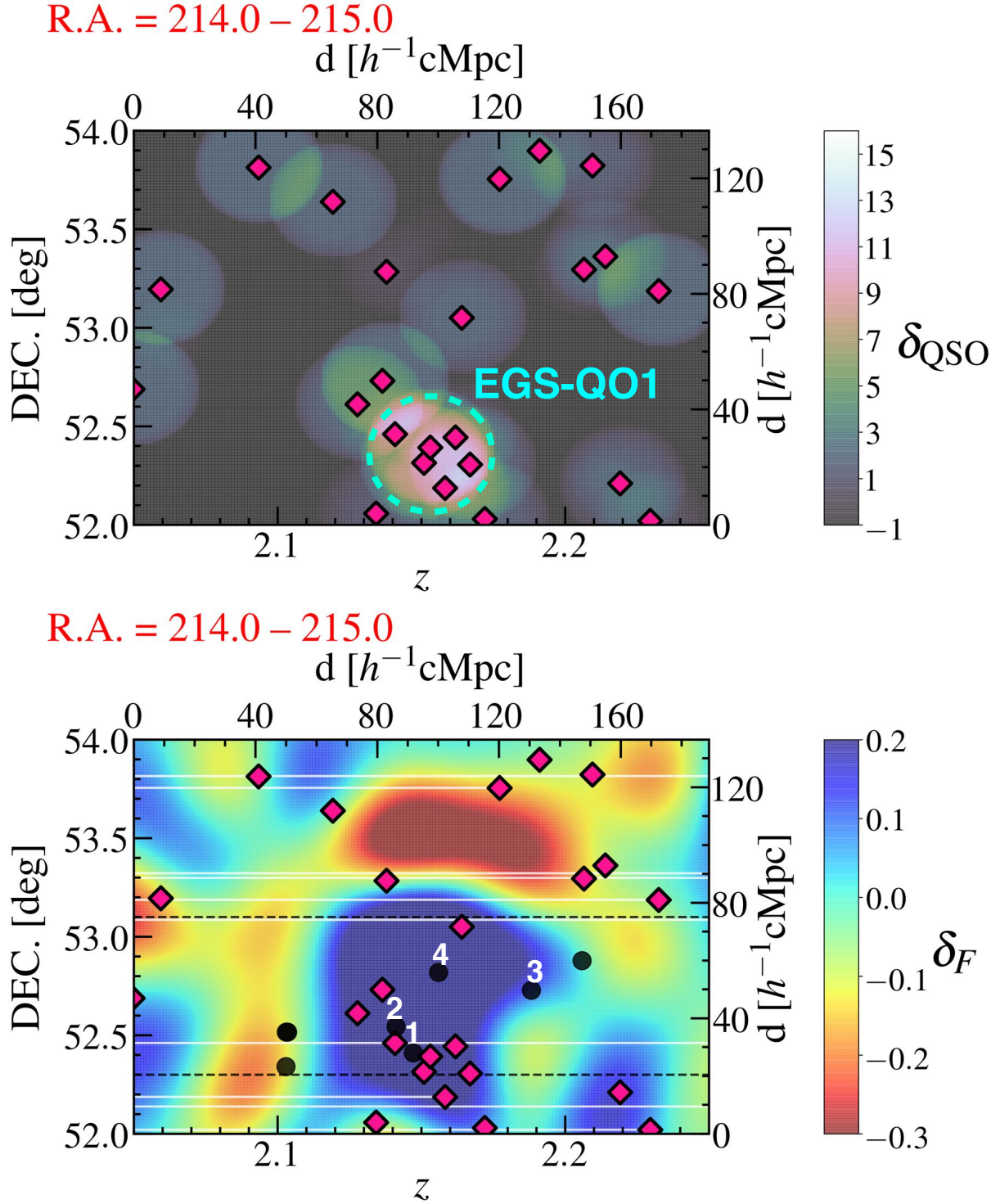


Figure 13. Top panel: Projection of the δ_{QSO} map for a $40 h^{-1} \text{ cMpc}$ (R.A. direction) slice in EGS that includes the EGS-QO1 QSO overdensity. The color contours represent the QSO overdensity δ_{QSO} , where white indicates a high δ_{QSO} value. The magenta diamonds represent the foreground QSOs (Section 2.2.1). The dashed circle indicates EGS-QO1, the identified QSO overdensity. Bottom panel: Same as the top panel, but for the HI tomography map. The width of the slice, $40 h^{-1} \text{ cMpc}$, is twice as large as the spatial resolution of this map (Section 3.2.2). The color contours represent the HI transmission overdensity δ_F , where the red (blue) color is a negative (positive) δ_F that corresponds to a strong (weak) HI absorption. The white dashed horizontal lines denote the background QSO sightlines. As in the top panel, the magenta diamonds represent the foreground QSOs (Section 2.2.1) residing in the slice. The black circles denote the positions of the LAEs (Section 2.1). The black dashed lines indicate the edges in declination of the LAE detections covered by the HETDEX survey. Although spatial correlations between objects (QSOs and LAEs) and HI absorption may be identified by visual inspection, one needs quantitative analysis (Section 4.2) to conclude the reality of the apparent spatial correlations.

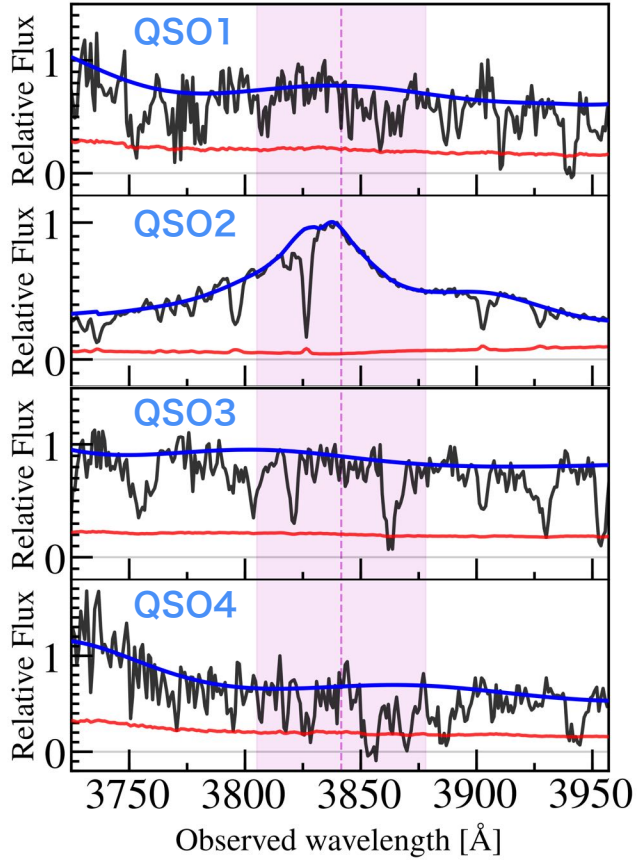


Figure 14. Spectra of the background QSO sightlines that probe the large HI underdensity around EGS-QO1. These background QSO sightlines are labeled QS01-4 in Figure 2. The black and red lines depict flux and error per pixel, respectively. The error is calculated from the errors of the flux measurements and the MF-PCA continuum fitting (Section 3.1.1). The blue curves are the estimated continua. The magenta dashed lines (shades) represent the wavelength center (range) that corresponds to the HI underdensity redshift (range) of $z = 2.16$ ($z = 2.13 - 2.19$). The background QSO sightlines indicate weak HI absorption within $z = 2.13 - 2.19$, although QS02 is not used in the wavelength range shown in this Figure for the HI tomographic map construction.

of $\sim 40 h^{-1} \text{ cMpc}$ at $\langle z \rangle = 2.16$. In fact, the galaxies and the QSOs in and around EGS-QO1 statistically show weak HI absorption. Because HI absorption is weakened in the EGS-QO1 QSO overdensity unlike in the blank field, we infer that the QSOs of EGS-QO1 probably produce an ionized bubble as a result of the overlap of multiple proximity zones of the QSOs, where a galaxy overdensity with a large HI-gas overdensity originally existed. This physical picture is illustrated in Figure 19 (b).

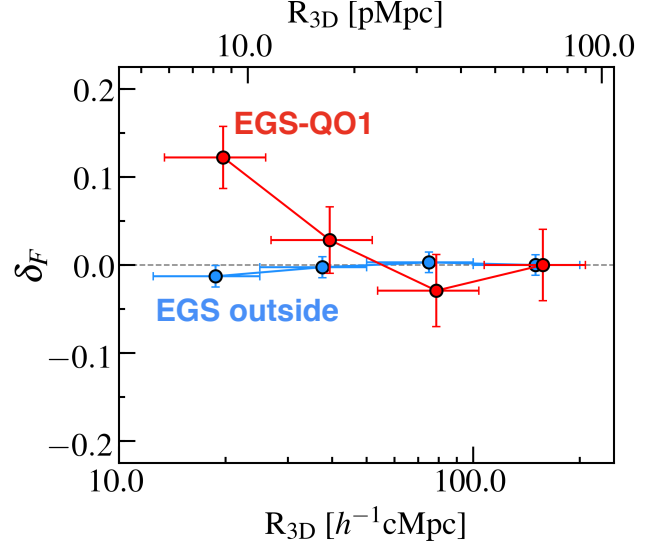


Figure 15. Same as Figure 11, but for the six QSOs forming the extreme QSO overdensity, EGS-QO1 (red circles). We overplot the HI radial profile of the 72 foreground QSOs that reside outside of the EGS-QO1 (i.e. EGS outside; blue circles). A large-scale HI transmission underdensity is found around the QSOs of EGS-QO1. It is noted that the EGS HI tomography map has a smoothing scale of $20 h^{-1} \text{ cMpc}$ and the HI radial profiles are constructed beyond $20 h^{-1} \text{ cMpc}$ diameter around QSOs.

The relationship between the physical pictures of Figure 19 (a) and (b) may be explained by evolution of photoionization of HI gaseous LSSs. A matter overdensity in LSSs produces the overdensities of HI gas and galaxies (Cai et al. 2017, 2016). Once QSO activity is triggered in the galaxies, HI gas in the overdensity is photoionized by photons from the QSOs (Mukae et al. 2020; Momose et al. 2020).⁹ This makes a cosmic volume of weak HI absorption corresponding to the ionized bubble. Note that again the ionized bubble has a low HI fraction that can be even smaller than that of the cosmic average HI fraction at $z \sim 2$ in the universe after cosmic reionization (Section 4.2).

6. SUMMARY

We have investigated IGM HI gas distributions around $z \sim 2$ galaxies in two galaxy environments: a blank field (COSMOS) and an extreme QSO overdensity field (EGS). Combining the large survey datasets of galaxies and QSOs that are provided by HETDEX LAEs and SDSS-IV/eBOSS QSOs, respectively, we construct the

⁹ A timeline of this evolutionary process is not clear. It may be possible for a large HI-gas overdensity (as in Figure 19 b) to form first almost completely, and that subsequently QSOs appear to ionize the HI gas. However, it is more likely that QSOs gradually ionize the HI gas at the assembly stage of the large HI-gas overdensity.

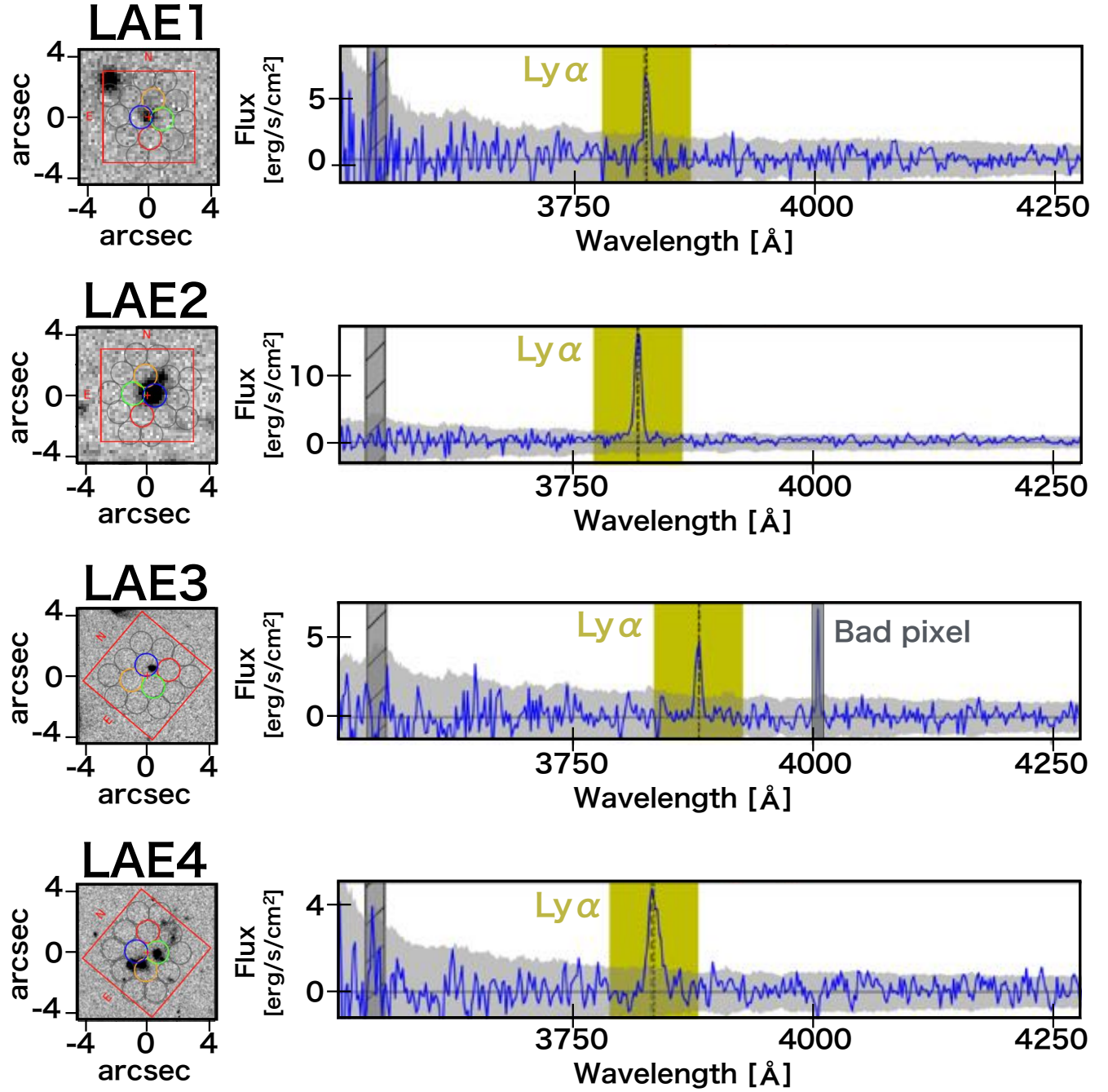


Figure 16. Right: HETDEX spectra of LAE1–4 residing in the extreme QSO overdensity EGS-QO1. The black dashed lines denote the wavelengths of the Ly α emission lines that are highlighted with the yellow shades. The light gray shades represent the 3 sigma noise levels. The dark gray shades present the wavelength range of bright sky lines and bad pixels. Left: HETDEX Fiber positions atop the broadband images taken with CFHT/MegaCam or HST/WFC3. The red, blue, green, and yellow circles present the positions and the sky coverage of the fibers used for the measurements of the LAE spectra.

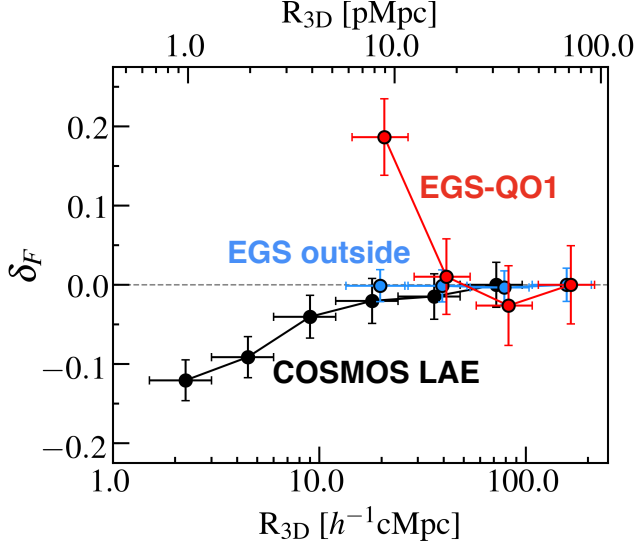


Figure 17. Same as Figure 11, but for the HI radial profile around LAE1–4 in the extreme QSO overdensity EGS-QO1 (red circles). The blue and black circles are the HI radial profiles of LAEs in the blank fields: the blue circles are the rest of 22 EGS LAEs that reside outside of the EGS-QO1 (i.e. EGS outside) and the black circles are the COSMOS LAEs. A significant HI transmission underdensity is identified around LAE1–4, which is similar to the one around the QSOs in EGS-QO1 (Figure 15).

samples of foreground galaxies and QSOs at $z \sim 2$ as well as the sample of background QSOs at $z > 2$. In the sample of foreground QSOs, we have identified the extreme QSO overdensity, EGS-QO1, consisting of six QSOs in a radius of $20 h^{-1} \text{ cMpc}$.

For the COSMOS field, we use the HI tomography map of Lee et al. (2018), while for the EGS field we reconstruct 3D HI LSSs by performing HI tomography based on HI absorption found in the spectra of background QSOs. These COSMOS and EGS HI tomography maps have cosmic volumes of $(30 \times 24 \times 444, 124 \times 136 \times 444) h^{-3} \text{ cMpc}^3$, respectively, at $z = 2.3$. We have investigated spatial correlations between the HI absorption and the galaxies in the two HI tomography maps. Our findings are listed below.

1. In the blank field of COSMOS that has no eBOSS QSOs within the volume of the tomography map, the spherically averaged HI radial profiles indicate that HI absorption around galaxies is stronger than those of the cosmic average at a distance from these galaxies up to $10 h^{-1} \text{ cMpc}$. Stronger HI absorption is found closer to the galaxies. The same trends are also found in the averaged 2D HI absorption map (transverse vs. LOS distances). These results suggest that the IGM HI gas and galaxies (LAEs) are spatially correlated, and that more HI gas exists around such galaxies.

2. In the averaged 2D HI absorption map shown in Figure 10, there is an anisotropy in the transverse and LOS directions. On average, the HI absorption peak is blueshifted by $\sim 200 \text{ km s}^{-1}$ from the galaxy $\text{Ly}\alpha$ redshift. This result independently reproduces the known average velocity offset between the $\text{Ly}\alpha$ emission redshift and the galaxy systemic redshift, using a completely independent tracer.
3. The extreme QSO overdensity of EGS-QO1 resides in an HI underdensity volume with a size of $\sim 40 \times 70 \times 40 h^{-3} \text{ cMpc}^3$ at $z = 2.13\text{--}2.19$ (centered at $\langle z \rangle = 2.16$). In this volume, the spherically-averaged HI radial profiles show that HI absorption around galaxies (and QSOs) is weaker than that of the cosmic average, and that the weaker HI absorption exists closer to the galaxies (and the QSOs). These results contrast with those of the blank fields of COSMOS and EGS outside of EGS-QO1. Interestingly, in the EGS HI tomography map, we identify an ionized bubble with a size of $\sim 40 h^{-1} \text{ cMpc}$ at $\langle z \rangle = 2.16$ in the volume of the EGS-QO1. The ionized bubble may form due to intense ionizing photon radiation as a result of the overlap of multiple proximity zones of the QSOs.
4. As noted above, we find possible opposite trends of the HI-galaxy spatial correlation in the two fields, the blank field and the extreme QSO overdensity field. A schematic illustration of our interpretation is shown in Figure 19. Although matter overdensities produce galaxies and galaxy+QSO overdensities, QSOs, if present, ionize the hydrogen gas around galaxies in the overdensity. In an extreme QSO overdensity, the negative correlation of the HI-galaxy spatial distribution is probably created by ionizing radiation of the QSOs. If our interpretation (Figure 19) is correct, the two different trends of HI-galaxy spatial correlation may be explained by evolution of photoionization in HI gaseous LSSs. In other words, once QSO activity emerges in galaxies residing in an HI gas overdensity, the HI gas around the galaxies is photoionized by the ionizing photons of the QSOs.

The evolutionary picture is based on one QSO overdensity (EGS-QO1). More QSO overdensities should be investigated to statistically test the picture as well as the morphology of giant ionized bubbles, because QSOs are actually complicated systems whose proximity zones relate to physical quantities such as the number of ionizing photons, the opening angle for ionizing photon escape, the lifetime, and the duty cycle (e.g., Bosman et al. 2020; Adelberger 2004). Further investigation will be made with forthcoming data from the HETDEX survey. Future data releases are expected to have improved spec-

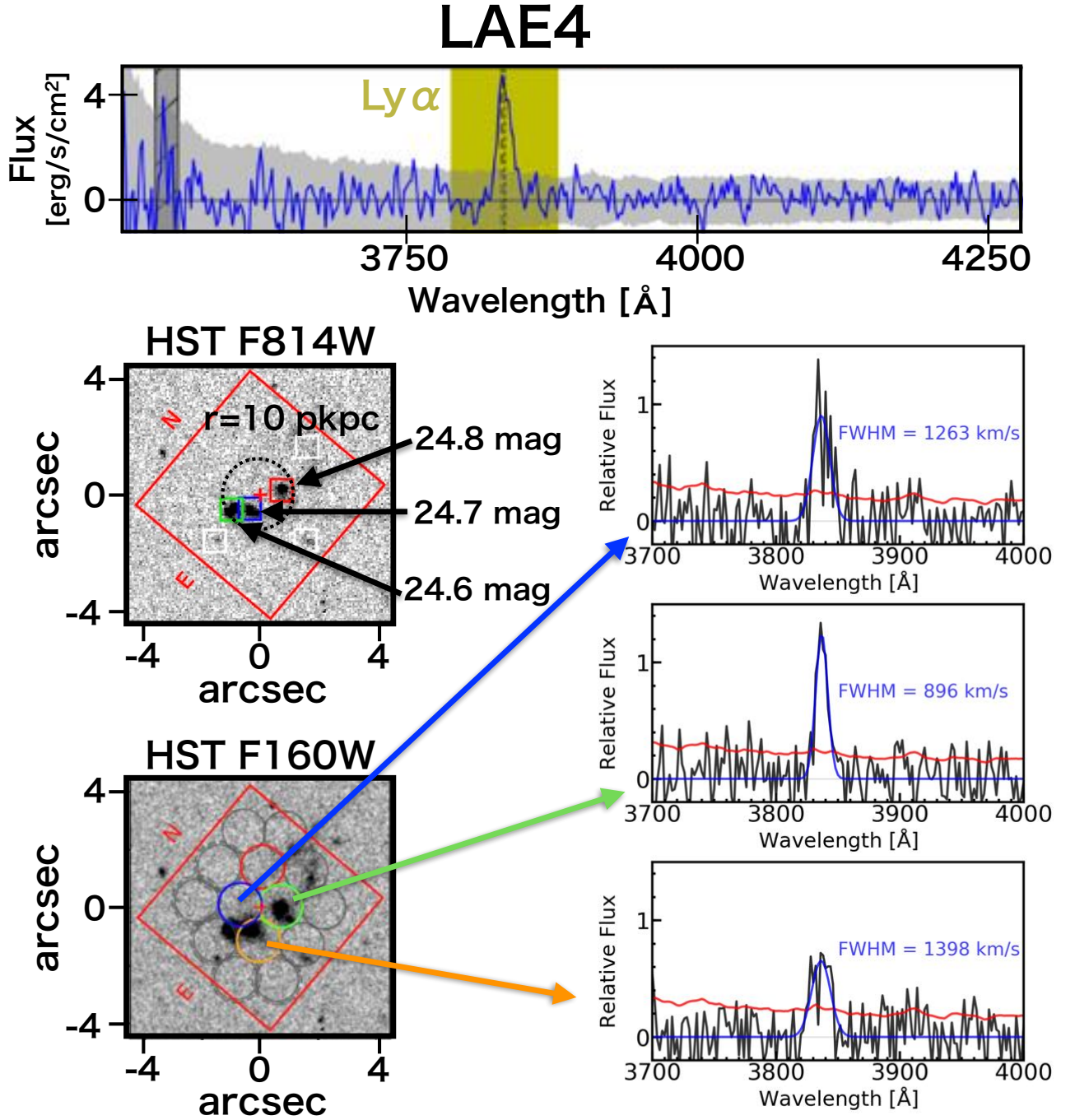


Figure 18. Top: the spectrum of the LAE4 over the HETDEX fibers. The black dashed line represents the wavelength of the Ly α emission line that is highlighted with the yellow shading. Middle: HST F814W image of LAE4. The red, blue, and green squares indicate positions of the triple-continuum components, all of which have similar F814W magnitudes, 24.8, 24.7, and 24.6 mag, respectively. The dashed circle (red cross) denotes the 10 pkpc circle (circle center) indicating the approximate size of the LAE4 system. Bottom: Positions and sky coverage of the HETDEX fibers, shown as circles on the HST F160W image. The spectra associated with the blue, green, and orange fibers have clear detections of Ly α emission lines that are presented in the spectrum panels on the right-hand side. In these spectrum panels, the black, red, and blue lines denote the spectra, the 1σ sky levels, and the best-fit Gaussian profiles to the Ly α emission lines, respectively. Note that the 1.5 arcsecond diameter fibers and the image quality of the HETDEX observation are much larger than the image sampling in the HST images, so the spectra of the three HST continuum image components are blended.

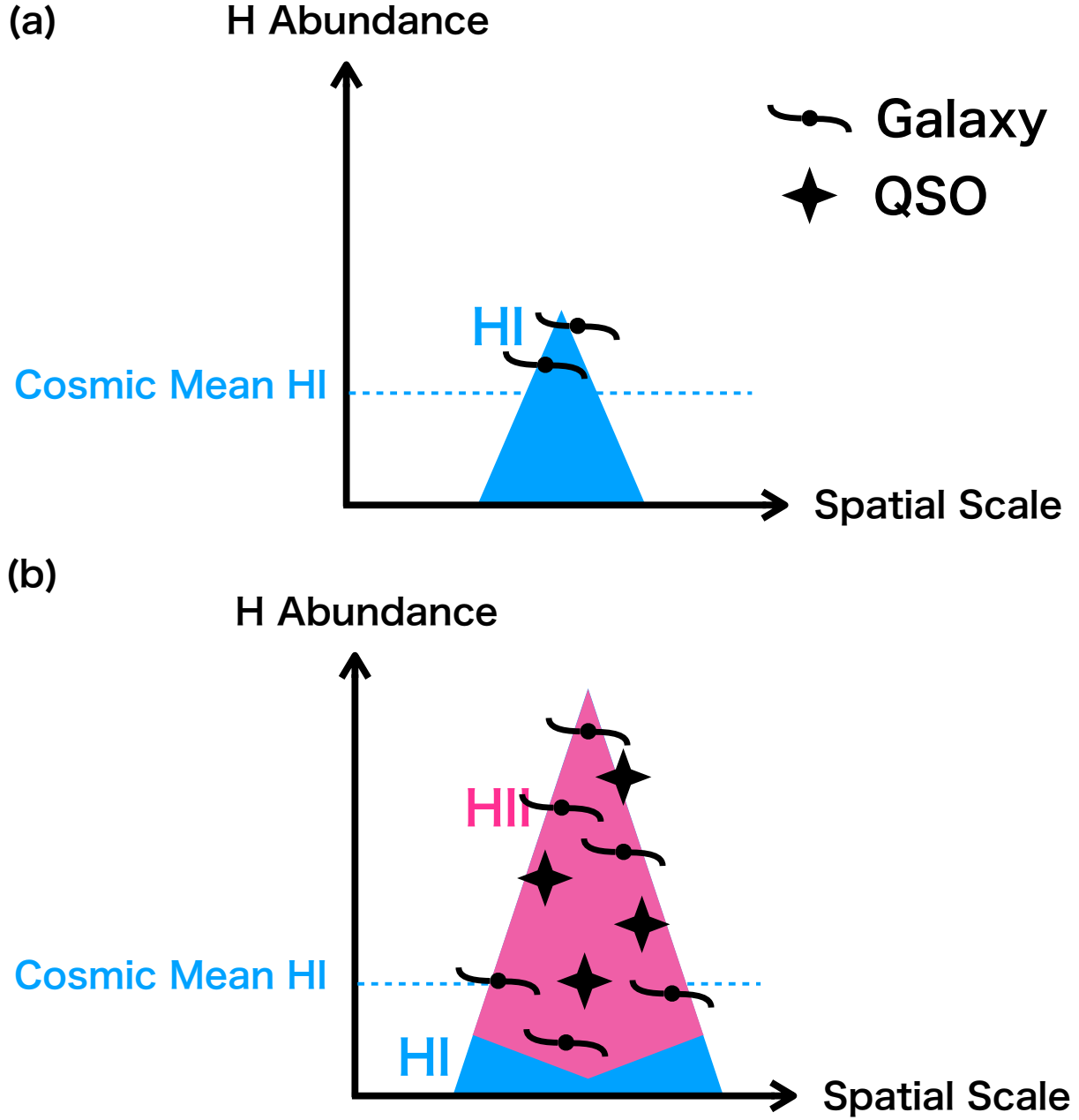


Figure 19. Schematic illustration of the physical picture suggested by this study. The images (a) and (b) show the ionized and neutral hydrogen gas around galaxies/QSOs with red and blue colors, respectively; (a) represents galaxies in an average blank field, while (b) indicates galaxies/QSOs in an extreme QSO overdensity.

tral traces, sky subtraction, cosmic-ray removal, and flux calibration (Gebhardt et al. 2020, in preparation). The HETDEX survey will ultimately provide 10^6 galaxies with spectroscopic redshifts at $z = 1.9\text{--}3.5$ in a 9 Gpc^3 volume. The HETDEX survey will statistically reveal the galaxy - IGM H I relation as a function of QSO overdensities in the large HETDEX Spring Field (300 deg^2 ; Hill & HETDEX Consortium 2016). Such statistical studies of LSS photoionization will shed light not only on the suppression of the formation of low-mass galaxies due to enhanced UVB radiation, but also the ionization processes of the intra-cluster media of galaxy clusters.

We thank the anonymous referee for constructive comments and suggestions that definitely improved the clarity of the paper. We are grateful to Koki Kakiichi, Sidhartha Gurung-Lopez, and Chris Sneden for their useful discussions and comments.

HETDEX is led by the University of Texas at Austin McDonald Observatory and Department of Astronomy with participation from the Ludwig-Maximilians-Universität München, Max-Planck-Institut für Extraterrestrische Physik (MPE), Leibniz-Institut für Astrophysik Potsdam (AIP), Texas A&M University, Pennsylvania State University, Institut für Astrophysik Göttingen, The University of Oxford, Max-Planck-Institut für Astrophysik (MPA), The University of Tokyo and Missouri University of Science and Technology. In addition to Institutional support, HETDEX is funded by the National Science Foundation (grant AST-0926815), the State of Texas, the US Air Force (AFRL FA9451-04-2-0355), and generous support from private individuals and foundations. The observations were obtained with the Hobby-Eberly Telescope (HET), which is a joint project of the University of Texas at Austin, the Pennsylvania State University, Ludwig-Maximilians-Universität München, and Georg-August-Universität Göttingen. The HET is named in honor of its principal benefactors, William P. Hobby and Robert E. Eberly. VIRUS is a joint project of the University of Texas at Austin, Leibniz-Institut für Astrophysik Potsdam (AIP), Texas A&M University, Max-Planck-Institut für Extraterrestrische-Physik (MPE), Ludwig-Maximilians-Universität München, The University of Oxford, Pennsylvania State University, Institut für Astrophysik Göttingen,, Max-Planck-Institut für Astrophysik (MPA) The Texas Advanced Computing Center

(TACC) at The University of Texas at Austin provided high performance computing, visualization, and storage resources that contributed to the research results reported within this paper.

The Institute for Gravitation and the Cosmos is supported by the Eberly College of Science and the Office of the Senior Vice President for Research at The Pennsylvania State University.

This paper is supported by World Premier International Research Center Initiative (WPI Initiative), MEXT, Japan, and KAKENHI (15H02064, 17H01110, and 17H01114) Grant-in-Aid for Scientific Research (A) through Japan Society for the Promotion of Science. S.M acknowledges support from the JSPS through the JSPS Research Fellowship for Young Scientists.

Funding for the Sloan Digital Sky Survey IV has been provided by the Alfred P. Sloan Foundation, the U.S. Department of Energy Office of Science, and the Participating Institutions. SDSS-IV acknowledges support and resources from the Center for High-Performance Computing at the University of Utah. The SDSS web site is www.sdss.org. SDSS-IV is managed by the Astrophysical Research Consortium for the Participating Institutions of the SDSS Collaboration including the Brazilian Participation Group, the Carnegie Institution for Science, Carnegie Mellon University, the Chilean Participation Group, the French Participation Group, Harvard-Smithsonian Center for Astrophysics, Instituto de Astrofísica de Canarias, The Johns Hopkins University, Kavli Institute for the Physics and Mathematics of the Universe (IPMU) / University of Tokyo, the Korean Participation Group, Lawrence Berkeley National Laboratory, Leibniz Institut für Astrophysik Potsdam (AIP), Max-Planck-Institut für Astronomie (MPIA Heidelberg), Max-Planck-Institut für Astrophysik (MPA Garching), Max-Planck-Institut für Extraterrestrische Physik (MPE), National Astronomical Observatories of China, New Mexico State University, New York University, University of Notre Dame, Observatório Nacional / MCTI, The Ohio State University, Pennsylvania State University, Shanghai Astronomical Observatory, United Kingdom Participation Group, Universidad Nacional Autónoma de México, University of Arizona, University of Colorado Boulder, University of Oxford, University of Portsmouth, University of Utah, University of Virginia, University of Washington, University of Wisconsin, Vanderbilt University, and Yale University.

REFERENCES

- Adelberger, K. L. 2004, *ApJ*, 612, 706
- Adelberger, K. L., Shapley, A. E., Steidel, C. C., et al. 2005, *ApJ*, 629, 636
- Adelberger, K. L., & Steidel, C. C. 2005, *ApJ*, 630, 50
- Becker, G. D., Hewett, P. C., Worseck, G., & Prochaska, J. X. 2013, *MNRAS*, 430, 2067
- Bielby, R. M., Shanks, T., Crighton, N. H. M., et al. 2017, *MNRAS*, 471, 2174

- Bosman, S. E. I., Kakiichi, K., Meyer, R. A., et al. 2020, *ApJ*, 896, 49
- Cai, Z., Fan, X., Peirani, S., et al. 2016, *ApJ*, 833, 135
- Cai, Z., Fan, X., Bian, F., et al. 2017, *ApJ*, 839, 131
- Caucci, S., Colombi, S., Pichon, C., et al. 2008, *MNRAS*, 386, 211
- Chiang, Y.-K., Overzier, R., & Gebhardt, K. 2013, *ApJ*, 779, 127
- . 2014, *ApJL*, 782, L3
- Conroy, C., & White, M. 2013, *ApJ*, 762, 70
- Davis, M., Guhathakurta, P., Konidaris, N. P., et al. 2007, *ApJL*, 660, L1
- Dawson, K. S., Kneib, J.-P., Percival, W. J., et al. 2016, *AJ*, 151, 44
- Dekel, A., Birnboim, Y., Engel, G., et al. 2009, *Nature*, 457, 451
- Dijkstra, M., Haiman, Z., & Spaans, M. 2006, *ApJ*, 649, 14
- D’Odorico, V., Bruscoli, M., Saitta, F., et al. 2008, *MNRAS*, 389, 1727
- Draine, B. T. 2011, *Physics of the Interstellar and Intergalactic Medium*
- Evans, C. J., Barbuy, B., Bonifacio, P., et al. 2012, in *Society of Photo-Optical Instrumentation Engineers (SPIE) Conference Series*, Vol. 8446, Ground-based and Airborne Instrumentation for Astronomy IV, 84467K
- Faucher-Giguère, C.-A., Prochaska, J. X., Lidz, A., Hernquist, L., & Zaldarriaga, M. 2008, *ApJ*, 681, 831
- Fox, A., & Davè, R. 2017, *Gas Accretion onto Galaxies*, Vol. 430 (Basel: Springer International Publishing AG), doi:10.1007/978-3-319-52512-9
- Hashimoto, T., Ouchi, M., Shimasaku, K., et al. 2013, *ApJ*, 765, 70
- Hennawi, J. F., Prochaska, J. X., Cantalupo, S., & Arrigoni-Battaia, F. 2015, *Science*, 348, 779
- Hill, G. J. 2014, *Advanced Optical Technologies*, 3, 265
- Hill, G. J., & HETDEX Consortium. 2016, in *Astronomical Society of the Pacific Conference Series*, Vol. 507, Multi-Object Spectroscopy in the Next Decade: Big Questions, Large Surveys, and Wide Fields, ed. I. Skillen, M. Barcells, & S. Trager, 393
- Hill, G. J., Gebhardt, K., Komatsu, E., et al. 2008, in *Astronomical Society of the Pacific Conference Series*, Vol. 399, Panoramic Views of Galaxy Formation and Evolution, ed. T. Kodama, T. Yamada, & K. Aoki, 115
- Hill, G. J., Kelz, A., Lee, H., et al. 2018a, in *Society of Photo-Optical Instrumentation Engineers (SPIE) Conference Series*, Vol. 10702, Proc. SPIE, 107021K
- Hill, G. J., Drory, N., Good, J. M., et al. 2018b, in *Society of Photo-Optical Instrumentation Engineers (SPIE) Conference Series*, Vol. 10700, Ground-based and Airborne Telescopes VII, 107000P
- Hinshaw, G., Larson, D., Komatsu, E., et al. 2013, *ApJS*, 208, 19
- Inoue, A. K., Shimizu, I., Iwata, I., & Tanaka, M. 2014, *MNRAS*, 442, 1805
- Jalan, P., Chand, H., & Srianand, R. 2019, *ApJ*, 884, 151
- Kakiichi, K., & Dijkstra, M. 2018, *MNRAS*, 480, 5140
- Kashikawa, N., Kitayama, T., Doi, M., et al. 2007, *ApJ*, 663, 765
- Kelz, A., Jahn, T., Haynes, D., et al. 2014, *Society of Photo-Optical Instrumentation Engineers (SPIE) Conference Series*, Vol. 9147, VIRUS: assembly, testing and performance of 33,000 fibres for HETDEX, 914775
- Kereš, D., Katz, N., Weinberg, D. H., & Davé, R. 2005, *MNRAS*, 363, 2
- Kikuta, S., Imanishi, M., Matsuoka, Y., et al. 2017, *ApJ*, 841, 128
- Kikuta, S., Matsuda, Y., Cen, R., et al. 2019, *PASJ*, 71, L2
- Lee, K.-G., Hennawi, J. F., White, M., Croft, R. A. C., & Ozbek, M. 2014a, *ApJ*, 788, 49
- Lee, K.-G., Suzuki, N., & Spergel, D. N. 2012, *AJ*, 143, 51
- Lee, K.-G., Bailey, S., Bartsch, L. E., et al. 2013, *AJ*, 145, 69
- Lee, K.-G., Hennawi, J. F., Stark, C., et al. 2014b, *ApJL*, 795, L12
- Lee, K.-G., Hennawi, J. F., White, M., et al. 2016, *ApJ*, 817, 160
- Lee, K.-G., Krolewski, A., White, M., et al. 2018, *ApJS*, 237, 31
- Leung, A. S., Acquaviva, V., Gawiser, E., et al. 2017, *ApJ*, 843, 130
- Liang, Y., Kashikawa, N., Cai, Z., et al. 2020, *arXiv e-prints*, arXiv:2008.01733
- McQuinn, M. 2016, *ARA&A*, 54, 313
- Meiksin, A. A. 2009, *Reviews of Modern Physics*, 81, 1405
- Mo, H., van den Bosch, F. C., & White, S. 2010, *Galaxy Formation and Evolution* (Cambridge: Cambridge Univ. Press)
- Momose, R., Shimasaku, K., Kashikawa, N., et al. 2020, *arXiv e-prints*, arXiv:2002.07335
- Mukae, S., Ouchi, M., Kakiichi, K., et al. 2017, *ApJ*, 835, 281
- Mukae, S., Ouchi, M., Cai, Z., et al. 2020, *ApJ*, 896, 45
- Muzahid, S., Schaye, J., Marino, R. A., et al. 2019, *arXiv e-prints*, arXiv:1910.03593
- Nagamine, K., Shimizu, I., Fujita, K., et al. 2020, *arXiv e-prints*, arXiv:2007.14253

- Neufeld, D. A. 1990, *ApJ*, 350, 216
- Newman, A. B., Rudie, G. C., Blanc, G. A., et al. 2020, *ApJ*, 891, 147
- Noterdaeme, P., Petitjean, P., Carithers, W. C., et al. 2012, *A&A*, 547, L1
- Oke, J. B., & Gunn, J. E. 1983, *ApJ*, 266, 713
- Ozbek, M., Croft, R. A. C., & Khandai, N. 2016, *MNRAS*, 456, 3610
- Palanque-Delabrouille, N., Magneville, C., Yèche, C., et al. 2013, *A&A*, 551, A29
- Pâris, I., Petitjean, P., Ross, N. P., et al. 2017, *A&A*, 597, A79
- Pâris, I., Petitjean, P., Aubourg, É., et al. 2018, *A&A*, 613, A51
- Pichon, C., Vergely, J. L., Rollinde, E., Colombi, S., & Petitjean, P. 2001, *MNRAS*, 326, 597
- Ramsey, L. W., Sebring, T. A., & Sneden, C. A. 1994, *Society of Photo-Optical Instrumentation Engineers (SPIE) Conference Series*, Vol. 2199, Spectroscopic survey telescope project, ed. L. M. Stepp, 31–40
- Ravoux, C., Armengaud, E., Walther, M., et al. 2020, *arXiv e-prints*, arXiv:2004.01448
- Shibuya, T., Ouchi, M., Nakajima, K., et al. 2014, *ApJ*, 788, 74
- Somerville, R. S., & Davé, R. 2015, *ARA&A*, 53, 51
- Song, M., Finkelstein, S. L., Gebhardt, K., et al. 2014, *ApJ*, 791, 3
- Stark, C. W., White, M., Lee, K.-G., & Hennawi, J. F. 2015, *MNRAS*, 453, 311
- Steidel, C., Martin, C., Prochaska, J. X., et al. 2009, in *astro2010: The Astronomy and Astrophysics Decadal Survey*, Vol. 2010, 286
- Steidel, C. C., Erb, D. K., Shapley, A. E., et al. 2010, *ApJ*, 717, 289
- Susa, H., & Umemura, M. 2000, *ApJ*, 537, 578
- . 2004, *ApJ*, 600, 1
- Suzuki, N., Tytler, D., Kirkman, D., O’Meara, J. M., & Lubin, D. 2005, *ApJ*, 618, 592
- Turner, M. L., Schaye, J., Crain, R. A., et al. 2017, *MNRAS*, 471, 690
- Turner, M. L., Schaye, J., Steidel, C. C., Rudie, G. C., & Strom, A. L. 2014, *MNRAS*, 445, 794
- Umehata, H., Fumagalli, M., Smail, I., et al. 2019, *Science*, 366, 97
- van de Voort, F. 2017, *Astrophysics and Space Science Library*, Vol. 430, The Effect of Galactic Feedback on Gas Accretion and Wind Recycling, ed. A. Fox & R. Davé, 301
- Viel, M., Schaye, J., & Booth, C. M. 2013, *MNRAS*, 429, 1734
- White, M., Myers, A. D., Ross, N. P., et al. 2012, *MNRAS*, 424, 933